# Temporal Large-Eddy Simulation

## Final Report for NASA Grant NAG1-02033

C. D. Pruett

*Department of Mathematics & Statistics,*

*James Madison University, Harrisonburg, VA 22807*

31 July 2004

# Abstract

In 1999, Stolz and Adams [Phys. Fluids **11** (1999)] unveiled a subgrid-scale model for LES based upon approximately inverting (defiltering) the spatial grid-filter operator and termed the approximate deconvolution model (ADM). Subsequently, the utility and accuracy of the ADM were demonstrated in *a posteriori* analyses of flows as diverse as incompressible plane-channel flow and supersonic compression-ramp flow. In a prelude to the current paper, a parameterized *temporal* ADM (TADM) was developed and demonstrated in both *a priori* and *a posteriori* analyses for forced, viscous Burger's flow. The development of a time-filtered variant of the ADM was motivated primarily by the desire for a unifying theoretical and computational context to encompass direct numerical simulation (DNS), large-eddy simulation (LES), and Reynolds averaged Navier-Stokes simulation (RANS). The resultant methodology was termed temporal LES (TLES). To permit exploration of the parameter space, however, previous analyses of the TADM were restricted to Burger's flow, and it has remained to demonstrate the TADM and TLES methodology for three-dimensional flow. For several reasons, plane-channel flow presents an ideal test case for the TADM. Among these reasons, channel flow is anisotropic, yet it lends itself to highly efficient and accurate spectral numerical methods. Moreover, channel-flow has been investigated extensively by DNS, and a highly accurate data base of Moser et al. [Phys. Fluids **11** (1999)] exists. In the present paper, we develop a fully anisotropic TADM model and demonstrate its utility in simulating incompressible plane-channel flow at nominal values of $Re_\tau = 180$ and $Re_\tau = 590$ by the TLES method. The TADM model is shown to perform nearly as well as the ADM at equivalent resolution, thereby establishing TLES as a viable alternative to LES. Moreover, as the current model is sub-optimal is some respects, there is considerable room to improve TLES.

## I. INTRODUCTION

While the formal linkage of the equations governing large-eddy simulation (LES) and Reynolds-averaged Navier-Stokes simulation (RANS) has been well established,[9,10] it is of interest to investigate whether this linkage can be extended practically by developing filtering and averaging procedures that yield mutually consistent solution fields among DNS, LES, and RANS. A possible unifying context for these methodologies is afforded by filter theory. However, the linkage between DNS, LES, and RANS may be more natural within the context of time-domain filtering rather than the traditional spatial filtering commonly used in LES. Accordingly, the present paper attempts to establish temporal large-eddy simulation (TLES) as a practical methodology for solving the temporally filtered Navier-Stokes (TFNS) equations using causal time-domain filters. TLES lies at the nexus of three relatively recent developments in subgrid-scale (SGS) modeling for LES: dynamical modeling, approximate deconvolution methods, and time-domain filtering. Each is discussed in some detail below.

### A. Dynamic Modeling

LES dates to the early 1960's, when it was first exploited for weather modeling. Summarizing Pope[22], LES consists of four conceptual steps: 1) decomposition of the field variables into resolved and unresolved scales of motion, denoted here by $\bar{u}(t,x)$ and $\tilde{u}(t,x)$, respectively; 2) derivation of the equations of motion for the resolved scales; 3) closure of the governing equations by modeling the residual-stress tensor; and 4) numerical solution of the closed governing equations. Only in the last step does discretization arise.

Steps 1) and 2) are accomplished by subjecting the flow-field variables and the Navier-Stokes Equations (NSE), respectively, to the same low-pass filter, conventionally termed the *grid* filter. The terminology is unfortunate, because the filter is applied prior to discretization; hence, we will refer instead to the *primary* filter. Filtering the nonlinear terms of the NSE generates *residual stresses*, which require modeling in step 3. The more common term for residual stress is subgrid-scale (SGS) stress, but for the reason stated previously, this too is misleading. More correctly, the residual stress is alternately referred to as the subfilter-scale (SFS) stress, a distinction made by Gullbrand[13]. In conventional LES, the primary filter is implicit; that is, it is conceptual and does not play an active role in the solution procedure (Step 4).

The original residual-stress models were of eddy-diffusivity type, of which the Smagorinsky model is the most well known. Eddy-diffusivity models suffer from a number of defects, among them the tendencies to be overly dissipative and to correlate poorly with exact residual stresses. A more subtle shortcoming of initial approaches to LES was that implicit filtering obscured the relationship between the filter and the model, so much so that, until relatively recently, it was widely accepted within the LES community that the choice of filter and the model were completely independent[21,26].

In an effort to overcome the shortcomings of conventional LES, Germano and coworkers[8] proposed the concept of dynamic modeling, which re-invigorated the LES community. Dynamic modeling involves two filters: the primary ("grid") filter, which is implicit, and the secondary ("test") filter, which is explicit. The Germano identity links the residual-stress tensor with two other tensors, one of which the resolved turbulent stress tensor, $\mathcal{L}_{ij}$, is computable by secondary filtering of the resolved velocity fields. The quantity $\mathcal{L}_{ij}$ can be considered a measure of ill-resolution, from which a localized dissipation parameter is derived. Thus, dynamic models are local in time and space in that dissipation is applied only when and where needed. Perhaps the greatest contributions of dynamic modeling are explicit filtering and local dissipation; however, dynamic models suffer some theoretical and practical shortcomings.

The advent of explicit filtering resulted in a careful examination of the relationship between the filter(s) and the model from several points of view: experimental[19], computational[24], and analytical[25,30]. All recent investigations concur that there is strong coupling between the filter and the exact residual stress. Far from being independent, the model and filter are intricately related to the point that there is one-to-one correspondence between the filter and the model[24,30]. A secondary motivation for the current work is to render that dependence explicit.

### B. Approximate Deconvolution Methods

Conventional LES has relied upon models that are phenomenologically based; that is, they are derived primarily on the basis of physical considerations. Recent recognition of the tight coupling between filter and model has spurred attempts to approximate the residual stress mathematically rather than to model it. Taylor-series analyses (Leonard[18], Bardina[4], Pruett et al.[25]) fall into this category, as do more recent deconvolution methods (Shah and Ferziger[29], Geurts[11], Domaradzki and Saiki[7], and Stolz and Adams[31]). A lucid review of deconvolution methods can be found in Adams and Stolz[2].

Deconvolution methods are based upon deconvolving (defiltering) the filtered flow fields (provided that the filter is invertible). Interestingly, the method enjoys its utility *because* it is approximate, not *despite* being approximate. In LES, one wishes to recover accurately only the resolved scales, which deconvolution enhances, while appropriately dissipating the energy of the unresolved scales, which the ADM method also accomplishes by secondary *regularization.* The (spatial) approximate deconvolution model (ADM) of Stolz and Adams[31] has performed remarkably well in *a posteriori* analyses of flows as diverse as incompressible plane-channel flow[32] and supersonic compression-ramp flow[33]. Moreover, the dissipation provided by the filter renders the method applicable for shock-capturing in high-speed compressible flows (Adams[1]).

### C. Time-Domain Filtering

As mentioned previously, LES has relied historically on spatial filtering to separate resolved from unresolved scales. However, at least in concept, time-domain filtering offers a number of advantages, which were outlined previously in Dakhoul and Bedford[6] and in Pruett[23]. For completeness, we compile some of the advantages below.

1. Time-domain filters naturally commute with differentiation operators; commutation error, however, is problematic for spatial filters, particularly on finite domains[5,35].

2. Spatial filtering is problematic for highly stretched meshes or unstructured grids; temporal filters, on the other hand, operate independently of spatial discretizations.

3. LES based upon temporal filtering (=TLES) permits consistent comparison with results from most physical (e.g., wind-tunnel) experiments, in which data are typically recorded and processed in the time domain.

4. Time domain filters are compatible with flow manipulation by localized (point) sources[6].

5. As will be shown, the reformulation of LES for time-domain filters (=TLES), yields a parameterized system of governing equations for which the temporal filter-width $\Delta$ appears as an explicit parameter.

6. Last and perhaps most important, time-domain filtering provides a natural and unifying context to encompass DNS, LES, and RANS methodologies.

Time-domain filtering for LES also presents some conceptual and practical disadvantages as well, which are deemed relatively minor and are discussed in context.

Surprisingly little effort has been expended toward the exploitation of time-domain filtering for LES. Dakhoul and Bedford[6] and Aldama[3] each considered mixed space-time filtering for LES. In recent years, attention has been given to pure time-domain filtering, and both Eulerian and Lagrangian temporal filters have been considered in lieu of spatial filters for LES. In 1996, Pruett[23] applied Eulerian time-domain filtering for *a priori* analysis of axisymmetric jet flow, and in 1999, Meneveau et al.[20] exploited a Lagrangian time-domain filter for LES and demonstrated the time-filtered method for LES of isotropic turbulence. In a prelude to the current paper[27], a parameterized temporal ADM (TADM) was developed and demonstrated in both *a priori* and *a posteriori* analyses for forced, viscous Burger's flow. The analyses were necessarily restricted to Burger's flow so that the parameter space could be fully explored. However, for the spatially one-dimensional problem, LES results agreed very well with temporally filtered DNS results, suggesting that TADM methodology should be further pursued, which is the intent of this paper.

In the present paper, we develop an anisotropic TADM model and demonstrate the model in large-eddy simulation of incompressible plane channel flow at nominal $Re_\tau = 180$ and 590. In the next section, causal filtering is discussed, a candidate filter is presented, and a differential form of the filter is derived. In Section III, the temporally filtered Navier-Stokes equations are presented. Section IV is devoted to nomenclature. Deconvolution methods are discussed in general in Section V, and a TADM model is developed. Results of a reference DNS of channel flow are presented in Section VI. Section VII presents results of TLES with the TADM and compares these results to results of the reference DNS. Relevant discussion follows in Section VIII. The paper closes with few concluding remarks and suggestions for future study in Section IX.

## II. CAUSAL FILTERING

Time-domain filters are classified as *causal* or *acausal*,[34] depending upon whether they are applicable to real-time or *a posteriori* data processing, respectively. The interest here lies in real-time applications to TLES for which only causal filtering is appropriate.

Let $f(t)$ be a continuous function of time $t$. A causal linear filter is readily constructed by the integral operator

$$\bar{f}(t;\Delta) = \int_{-\infty}^{t} G(\tau - t;\Delta) f(\tau) d\tau, \tag{1}$$

where $G$ is a parameterized *filter kernel*, and the parameter $\Delta$ is the termed the *filter width.* (The convention of using semicolons to separate parameters from independent variables in argument lists is adopted here.)

The following properties of admissible kernels were discussed in[27], but are repeated here for completeness.

$$G(t;\Delta) \equiv \frac{1}{\Delta} g\left(\frac{t}{\Delta}\right), \tag{2}$$

where $g$ is any integrable function such that

$$g(t) \geq 0, \qquad \int_{-\infty}^{0} g(t) dt = 1 \quad \text{and} \quad g(0) = 1. \tag{3}$$

The non-negativity and normalization constraints in Eq. (3) imply that

$$\lim_{t \to -\infty} g(t) = 0, \tag{4}$$

and suffice for $G$ to approach a Dirac delta function as its parameter $\Delta \to 0$; that is,

$$\begin{aligned} \lim_{\Delta \to 0} \bar{f}(t;\Delta) &= \lim_{\Delta \to 0} \int_{-\infty}^{t} G(\tau - t;\Delta) f(\tau) d\tau \\ &= \int_{-\infty}^{t} \delta(\tau - t) f(\tau) d\tau \\ &= f(t). \end{aligned} \tag{5}$$

In[27], two examples of causal filters satisfying the constraints above were presented: a Heaviside filter and an exponential filter. Here, we restrict attention to the exponential filter (for reasons soon to be demonstrated). For the exponential kernel

$$g(t) = \exp(t) \to G(t;\Delta) = \frac{\exp(t/\Delta)}{\Delta}, \tag{6}$$

and the resulting integral operator in Eq. (1) is

$$\bar{f}(t;\Delta) = \frac{1}{\Delta}\int_{-\infty}^{t} \exp\left(\frac{\tau - t}{\Delta}\right) f(\tau)d\tau. \tag{7}$$

A drawback of the integral formulation just presented is the need to retain the long-time history of the solution field. However, by considering instead the differential form of the filter operator, storage requirements are reduced significantly, subject to the intrinsic storage needs of the numerical time-advancement scheme itself (for example, low-storage Runge-Kutta). By using Leibniz' rule to differentiate Eq. (7) with respect to time, the differential form of the exponential filter is obtained, namely

$$\frac{\partial}{\partial t}\bar{f}(t;\Delta) = \frac{f(t) - \bar{f}(t;\Delta)}{\Delta}. \tag{8}$$

The effect of a causal filter is most apparent from its transfer function $H(\Omega)$, which quantifies its amplitude and phase effects in Fourier space as a function of dimensionless frequency $\Omega = \omega\Delta$, where $\omega$ is the (dimensional) circular frequency. The transfer function of the continuous exponential filter is shown in Fig. 1. When causal filtering is applied to a temporally discretized problem with a time increment of $\Delta t$, the action of the filter is naturally parameterized by the filter-width ratio $r$ defined as

$$r = \frac{\Delta}{\Delta t}. \tag{9}$$

For the exponential filter, the parameterized transfer function is

$$\begin{aligned} H(\omega\Delta t;r) &= \frac{1}{1 + \imath r\omega\Delta t} && \text{(10a)} \\ & && \text{(10b)} \end{aligned}$$

Figure 2 presents the modulus of the transfer function of the exponential filter for selected values of the filter-width ratio. Note that $\omega\Delta t = \pi$ corresponds to a sampling rate at the Nyquist frequency, and that filtering at $\Omega > \pi$ is disallowed because it results in unacceptable aliasing error. Note also that $r = 0$ yields $H(\omega\Delta t; 0) = 1$, which eliminates the filter.

The filter-width ratio, $r$, is the only parameter of the differential filter. In general, the larger the value of $r$, the more dissipative the filter. (In this context, a "dissipative" low-pass filter is one with significant and broad-band attenuation of high-frequency Fourier harmonics.) The differential equation remains viable for all values of filter-width ratio ($0 < r$). However, whenever $r \approx 0$, the evolution equation becomes stiff, and small time steps are necessary for stability of the numerical integration scheme. The action of the parameterized differential filter on a spectrally rich time signal can be found in Fig. 5 of Reference[27].

Normally, when a continuous low-pass filter is discretized, the transfer function of the discrete filter deviates substantially from that of the continuous prototype, particularly at high frequencies. This is not the case, however, when the continuous filter is expressed in differential form, and the differential form is integrated in time by a high-order numerical scheme. For example, Fig. 3 compares the transfer function of the continuous exponential filter for $r = 1$ with that of the discrete filter obtained by solving Eq. 8 by the classical fourth-order Runge-Kutta method with a time-step $\Delta t$ that exactly satisfies the Nyquist criterion at the highest frequency. The continuous and discrete transfer functions are nearly indistinguishable. Surprisingly, the agreement improves as the filter-width ratio $r$ increases. Thus, for present purposes, it suffices to base subsequent analyses on the properties of the continuous differential filter.

## III. TEMPORALLY FILTERED NAVIER-STOKES EQUATIONS

The application of a causal temporal filter (e.g., Eq. (1)) to the Navier-Stokes equations (NSE) leads to the temporally filtered Navier-Stokes Equations (TFNSE), namely

$$\frac{\partial \overline{u}_j}{\partial x_j} = 0 \tag{11}$$

$$\frac{\partial \overline{u}_i}{\partial t} + \frac{\partial (\overline{u}_i \overline{u}_j)}{\partial x_j} = -\frac{\partial \overline{p}}{\partial x_i} + \frac{1}{Re}\frac{\partial^2 \overline{u}_i}{\partial x_j \partial x_j} - \frac{\partial R_{ij}}{\partial x_j}, \tag{12}$$

where $u_j$ is the velocity, $p$ is the pressure, and $Re$ is the Reynolds number. An overbar denotes a quantity that has been subjected to filtering by the primary filter, which is causal, and $R_{ij}$ represents the exact temporal residual-stress tensor defined as

$$R_{ij} \equiv \overline{u_i u_j} - \overline{u}_i \overline{u}_j. \tag{13}$$

Provided that filtering and differentiation operations commute, the TFNS equations are *formally* identical to the spatially filtered Navier-Stokes equations. As pointed out previously by Pruett,[23] commutativity is natural for temporal filters but remains problematic for spatial ones[5,35]. In general, for spatial *or* temporal primary filters, the residual stress depends strongly upon the filter, particularly upon its filter width and order property, which influence both the magnitude and the distribution of the residual stress. Because the exact residual stress depends upon the filter width, it is sometimes helpful to explicitly denote by $R_{ij} = R_{ij}(\Delta)$. In particular, it can be shown by Taylor-series analysis (e.g.,[25]), that $R_{ij}$ is of leading order $\Delta^2$ for first- or second-order primary filters.

The invariance properties of the TFNSE are discussed in detail in Section IIIa of Reference[27].

## IV. NOMENCLATURE

Because TLES represents a departure from the norm, it is advisable to define all terms and quantities precisely in the current context, which is the purpose of this section. To those for whom the discussion may seem pedantic, we apologize.

### A. Ensemble Mean and Long-Time Average

Let $E\{u_i\}$ denote the *ensemble mean* (or the *expected value*) of the velocity component $u_i$. Accordingly, the Reynolds decomposition of the velocity is given by

$$u_i = E\{u_i\} + u_i' \tag{14}$$

which partitions the velocity into time-independent and time-dependent contributions denoted the *mean* and *fluctuation*, respectively. Turbulence modeling efforts focus on the Reynolds-stress tensor $\tau_{ij} = E\{u_i'u_j'\}$, which, by virtue of the Reynolds decomposition, is given by

$$\tau_{ij} = E\{(u_i - E\{u_i\})(u_j - E\{u_j\})\} \tag{15}$$

By the ergodic hypothesis, for a statistically steady (stationary) flow, the ensemble mean of a turbulent quantity is equivalent to its long-time average, denoted hereafter by angle brackets. For stationary flow, for example, $< u_i >= E\{u_i\}$. In principle, the long-time average of a quantity is a constant computed by averaging over infinite time. In practice, it suffices to average over many integral time scales ($\bar{\tau}$). If the flow is homogeneous, the temporal interval necessary to compute the long-time average is reduced significantly by averaging also in homogeneous dimensions. As will be shown, channel flow is homogeneous in streamwise ($x$) and spanwise ($y$) extents. Consequently, in present parlance, $<>$ denotes either $<>_t$ or $<>_{t,x,y}$, where the time interval in either case is chosen sufficiently long to yield an accurate mean. In contrast, $<>_{x,y}$ denotes instantaneous averages over homogenous planes.

For channel flow, all field variables are either statistically symmetric or antisymmetric about the mid-plane. Due to the random influences of initial data, simulations produce slight asymmetries. However, because upper and lower channel halves represent different realizations, it is appropriate to average symmetrically about the channel mid-plane. Symmetric averages further reduce the time interval necessary to acquire an accurate mean and are exploited herein.

Henceforth, we presume that the flow is fully turbulent and stationary, in which case the Reynolds stress is defined alternately as

$$\tau_{ij} = < (u_i - < u_i >)(u_j - < u_j >) > \tag{16}$$

$$= < u_i u_j > - < u_i >< u_j > \tag{17}$$

where Eq. 17 exploits the properties that $<< a >>=< a >$, $< ca >= c < a >$, and $< a+b >=< a > + < b >$ for any time-dependent fields $a$ and $b$ and time-independent field $c$.

### B. Resolved and Sub-Filter Scales

For TLES, a natural decomposition of the velocity field $u_i$ is given by

$$u_i = \bar{u}_i - \tilde{u}_i \tag{18}$$

where the first and second terms on the right-hand side of Eq. 18 are termed the *resolved* and *sub-filter scale* (SFS) velocities, respectively. (Because the TFNSE are continuous and have yet to be discretized, we prefer the terminology *sub-filter scale* of Gullbrand[13] rather than the conventional but somewhat misleading term *sub-grid scale* (SGS).) It is worth noting, that, in general, unlike $< u_i >$, $\bar{u}_i$ is time-dependent.

In order to formally link RANS and TLES methodologies, we now wish to examine the relationship between the Reynolds stress (Eq. 17) and the (temporal) residual stress (Eq. 13). The reader is reminded that, unlike the Reynolds stress, the residual stress is a time-dependent function, parameterized by the filter width $\Delta$.

In TLES the solution variables are the resolved velocities $\bar{u}_i$. Consequently, the exact Reynolds stress is unavailable from the solution; the analogous computable quantity is the *resolved-scale Reynolds stress* $\bar{\tau}_{ij}$ defined as follows:

$$\begin{aligned}\bar{\tau}_{ij} &= < (\bar{u}_i - < \bar{u}_i >)(\bar{u}_j - < \bar{u}_j >) > && (19)\\ &= < \bar{u}_i\bar{u}_j > - < \bar{u}_i >< \bar{u}_j > && (20)\end{aligned}$$

### C. Exact TLES

As a sort of thought experiment, we now consider exact TLES; that is, TLES conducted with an exact residual-stress model. In exact TLES, the Reynolds stress is exactly the sum of the resolved-scale Reynolds stress and the mean residual stress; i.e.,

$$\begin{aligned}\tau_{ij} &= < u_i u_j > - < u_i >< u_j > \\ &= < \overline{u_i u_j} > - < \bar{u}_i >< \bar{u}_j > \qquad (21)\\ &= [< \overline{u_i u_j} - \bar{u}_i\bar{u}_j >] + [< \bar{u}_i\bar{u}_j > - < \bar{u}_i >< \bar{u}_j >] \\ &= < R_{ij} > + \bar{\tau}_{ij}\end{aligned}$$

Of the two contributions to the exact Reynolds stress, denoted above by bracketed terms, the first, the resolved-scale Reynolds stress, is computable from the solution, whereas, the second, the residual stress, must ultimately be modeled. For the moment, we presume the residual-stress model to be exact. Still, it may not be immediately clear why Eq. 21 is identical to Eq. 17. First, it is useful to note that Eq. 21 is exact in the limiting cases as $\Delta \to 0$ and $\Delta \to \infty$. By virtue of Eq. 5, $\bar{u}_i \to u_i$ and $\overline{u_i u_j} \to u_i u_j$ as $\Delta \to 0$. Hence, in the limit of vanishing $\Delta$, the mean residual stress (bracketed term 2 of the second line of Eq. 21) vanishes as the resolved-scale Reynolds stress (term 1 above) tends toward the exact Reynolds stress. On the other hand, it was shown in Reference[27] that the residual stress tends asymptotically toward the Reynolds stress as $\Delta \to \infty$; that is, $\lim_{\Delta\to\infty} R_{ij} = \tau_{ij}$ for a stationary flow, this by virtue of the fact that $\lim_{\Delta\to\infty} \bar{f}(t;\Delta) =< f(t) >$ for causal low-pass filters. Consequently, in the infinite limit, the first bracketed term in Eq. 21 tends toward $<< u_i >< u_j >> - < u_i >< u_j > = 0$; that is, the resolved-scale Reynolds stress vanishes. For finite $\Delta$, the last line of Eq. 21 is also identical to Eq. 17, for the reason that, in exact TLES, $< \bar{u}_i > = < u_i >$, because low-pass temporal filtering preserves the mean.

For conventional (spatial) LES, it is customary to validate the results against filtered DNS results; that is, by *a posteriori* analysis. For spatial LES, it suffices to spatially filter the DNS results at instants in time and then average over relatively few time steps. In contrast, *a posteriori* analysis for TLES requires real-time or *ex post facto* temporal filtering of DNS data over many time steps. Thus, to conduct *a posteriori* analyses for TLES, one would be forced into DNS with the substantial computational overhead associated with real-time implementation of the SFS model or with the enormous storage overhead associated with storing most or all time steps. Fortunately (provided the SFS model is adequate), Eq. 21 obviates the need for *a posteriori* analysis altogether, because it provides a mechanism by which to compare TLES results directly with DNS results without the need to filter the latter. *Indeed, this is an advantage of TLES relative to spatial LES, because conventional LES provides no means for directly comparing LES and DNS or LES and experiment.*

To summarize, the situation is thus. In TLES, the Reynolds stress is partitioned into two parts: the resolved-scale Reynolds stress $\bar{\tau}_{ij}$, which can be computed from the solution of the TFNSE, and the residual stress $R_{ij}$, which must be modeled. The exact partitioning depends on the temporal filter width $\Delta$. For vanishing filter width, all the Reynolds stress is contained in resolved scales, the residual stress vanishes identically, the TFNSE reduce to the NSE, and the simulation is equivalent to DNS. In the limit of infinite filter width, all the Reynolds stress is contained in sub-filter scales (i.e., in the residual stress), the resolved-scale Reynolds stress vanishes identically (because the field variables are time independent), the TFNSE reduce to the RANS equations (for stationary flow), and the simulation is equivalent to RANS, provided that the residual-stress model tends toward a Reynolds-stress model. In short, *the larger* $\Delta$, *the greater the burden placed on the model* $M_{ij} \approx R_{ij}$, *but also the greater the potential for grid coarsening.*

Finally, we consider the instantaneous *turbulent kinetic energy*, $k(t)$, defined here as

$$k(t) = \frac{1}{2}\int_{-1}^{+1} < u_i u_i >_{x,y} dz \tag{22}$$

The analogous computable quantity for TLES is the *resolved turbulent kinetic energy*, $\bar{k}(t)$

$$\bar{k}(t) = \frac{1}{2}\int_{-1}^{+1} < \bar{u}_i \bar{u}_i >_{x,y} dz \tag{23}$$

Also of interest is the *residual turbulent kinetic energy*, $k_R(t)$

$$k_R(t) = \frac{1}{2}\int_{-1}^{+1} < R_{ii} >_{x,y} dz \tag{24}$$

For exact TLES, the instantaneous sum of resolved and residual turbulent kinetic energies is (only) approximately $k(t)$. That is,

$$k(t) \approx \bar{k}(t) + k_R(t) \tag{25}$$

The time mean of the previous approximation, however, yields an exact equality; that is, $k = < k(t) > = < \bar{k}(t) > + < k_R(t) >$.

## V. DECONVOLUTION METHODS

As suggested in the Introduction, deconvolution methods seek to approximate $R_{ij}$ primarily by mathematical means rather than to model $R_{ij}$ by physical considerations. In this section, deconvolution methods are summarized briefly, the classical (spatial) ADM is presented, the ADM method is adapted for causal filters, and difficulties associated with causal filtering are addressed.

### A. Approximate Deconvolution

A lucid review of deconvolution methods can be found in Adams and Stolz[2], to which the reader is referred for details. Here, for completeness, we review the essentials.

Let $\hat{u}_j(\xi)$ be the temporal or (one-dimensional) spatial Fourier transform of the velocity field $u_j$, where $\xi = \kappa\Delta$ or $\xi = \omega\Delta$ for spatial or temporal filters, respectively, and where $\kappa$ is the wavenumber and $\omega$ is the circular frequency. Accordingly, $\Delta$ is either the spatial or temporal filter width. The Fourier transform of a filtered field is given by

$$\hat{\bar{u}}_j(\xi) = H(\xi)\hat{u}_j(\xi) \tag{26}$$

where $H$ is the transfer function of the filter (e.g., Fig. 1). If $H \neq 0$, the filter is said to be *invertible*, in which case

$$\hat{u}_j(\xi) = H^{-1}(\xi)\hat{\bar{u}}_j(\xi) \tag{27}$$

Using a standard trick from complex analysis,

$$H^{-1} = \frac{1}{1-(1-H)} = 1 + (1-H) + (1-H)^2 + \ldots + (1-H)^p + \ldots \tag{28}$$

The geometric series on the right of Eq. 28 converges provided $|1 - H| < 1$. Truncating the series at finite order $p$ yields an approximate inverse $\tilde{H}^{-1}$ of the transfer function, namely

$$\tilde{H}^{-1} = 1 + (1 - H) + (1 - H)^2 + ... + (1 - H)^p \tag{29}$$

If $\tilde{H}^{-1}$ were exact, then $\tilde{H}^{-1} * H = 1$, and all scales would be faithfully recovered from the filtered fields. Exact inversion is *not* desirable for present purposes. Rather, one desires to recover the resolved scales $0 \leq |\xi| \leq \xi_c$ exactly, but to appropriately dissipate the energy in the unresolved scales $\xi_c < |\xi| < \pi$. Thus, for LES or TLES, the ideal is that $H * \tilde{H}^{-1}$ approximates a sharp cutoff at $\xi_c$ in Fourier space.

Let $F$ represent the filter operator in physical space, and let $F^k$ denote a $k$-times iterated filtering operation. That is;

$$\begin{aligned} \bar{u}_j &= F u_j \\ \bar{\bar{u}}_j &= F \bar{u}_j = F^2 u_j \\ &\cdots \\ \bar{u}_j^{(k)} &= F^k u_j \end{aligned} \tag{30}$$

By isometry between physical and Fourier space (Stolz and Adams[31]), Eq. 29 can be exploited to yield a deconvolution scheme in physical space, namely

$$\begin{aligned} u_j &\approx v_j = [I + (I - F) + (I - F)^2 + ... + (I - F)^p]\bar{u}_j \\ &= \sum_{k=0}^{p} c_k \bar{u}_j^{(k+1)} \end{aligned} \tag{31}$$

where $v_j$ is the $p$th-order deconvolution approximation of $u_j$, and where the coefficients $c_k$ are readily determined to any order $p$ by the binomial formula. Equation 31 represents but one of many possible approximate deconvolution techniques (See Adams and Stolz[2]); however, it is advantageous in being linear and involving only multiply filtered quantities. For specificity, approximate deconvolutions of orders $p = 0$, $p = 1$, and $p = 2$ are given below.

$$\begin{aligned} v_j &= \bar{u}_j \quad (p = 0) \\ v_j &= 2\bar{u}_j - \bar{\bar{u}}_j \quad (p = 1) \\ v_j &= 3\bar{u}_j - 3\bar{\bar{u}}_j + \bar{\bar{\bar{u}}}_j \quad (p = 2) \end{aligned} \tag{32}$$

### B. Spatial Approximate Deconvolution Method

Stolz et al.[32] present two anisotropic spatial ADMs, which are reproduced below (in current parlance) for completeness.

$$[M_1]_{ij} \equiv \overline{v_i v_j} - \bar{u}_i \bar{u}_j \tag{33}$$

$$[M_2]_{ij} \equiv \overline{v_i v_j} - \bar{v}_i \bar{v}_j \tag{34}$$

Model $M_2$ reduces to the scale similarity model (SSM) of Bardina[4] for $p = 0$ and accordingly is dubbed the generalized SSM (GSSM). Although Stolz and Adams find little difference between the two models in practical applications, only the latter is suited for TLES, for reasons addressed subsequently.

It is well known that models of similarity type provide too little dissipation for practical applications to LES. The ADMs suffer from a similar deficiency without *secondary regularization*, a type of high-order artificial dissipation that is accomplished by introducing a relaxation term to the right-hand sides of each momentum equation. In physical space, the relaxation term is of the form

$$-\chi(\bar{u}_j - \bar{v}_j) \tag{35}$$

where $\chi$ is an arbitrary non-negative parameter, to which the solution is not very sensitive[32]. In Fourier space, the relaxation term becomes

$$-\chi(I - H * \tilde{H}^{-1}) * \hat{\bar{u}}_j \tag{36}$$

Provided $(I - H * \tilde{H}^{-1})$ is positive semi-definite, which is the case for symmetric spatial filters, the relaxation term is dissipative for all unresolved Fourier components.

In the original spatial ADM, the cutoff is fixed at $\xi_c = 2/3\pi$. For this value, Stolz et al.[32] report the ADM to give acceptable results for $p = 3$ and that deconvolution orders above 5 do not significantly improve its performance. Consequently, they fix the deconvolution order at $p = 5$. Stolz et al. also observe that secondary regularization is equivalent to imposing a high-order filter upon the solution. According to Stolz et al.[32], the effective order of the secondary filter is the product of the order of the primary filter and the order of the deconvolution plus one. For example, for the spatial ADM of Reference[32], which exploits a 4th-order compact-difference filtering and $p = 5$, the secondary filter is formally of order 24. Thus, in the classical ADM method, secondary regularization acts virtually as spectral filtering.

### C. Temporal Approximate Deconvolution Method

The proposed temporal ADM (TADM) is formally identical to the second of the ADMs proposed by Stolz et al.; that is, Eq. 34, where $v_j$ is given by the truncated geometric series Eq. 31, except, of course, that now $F$ denotes a causal filter operator. Because phase error introduced by temporal filtering results in the first and second terms of Eq. 33 being out of phase respective to one another, only the second ADM model (Eq. 34) is viable for present purposes (TLES). Henceforth, we refer symbolically to the residual stress modeled by the temporal version of $[M_2]_{ij}$ simply as $M_{ij}$. The TADM also exploits secondary regularization formally identical to Eq. 35.

Recall that Eq. 28, from which Eq. 31 is obtained, converges only for $|1 - H| < 1$. Fig 4 shows this quantity for both the exponential filter of current interest and the Heaviside filter of Section II of Reference[27]. For the exponential filter $|1 - H(\xi)| < 1$ for all $0 \leq \xi < \infty$. In contrast, this constraint is violated for high $\xi$ for the Heaviside filter. Consequently, the Heaviside filter is not a viable candidate for temporal deconvolution techniques of this type. Henceforth, we consider only the exponential filter (while recognizing that other filters yet to be examined could be superior in many respects).

### D. Adaptations of Original ADM for Temporal Deconvolution

Straightforward adaptation of approximate deconvolution (Eq. 29) for the TADM is problematic, chiefly due to the phase error generated by causal filtering. (These difficulties were partially masked in the Burger's flow considered previously by the authors[27], because of the intrinsic physical dissipation present at low Reynolds number.) For spatial filtering with a centered stencil, $H$, $\tilde{H}^{-1}$, and $H * \tilde{H}^{-1}$ are each purely real, and the operator $H * \tilde{H}^{-1}$, which is exploited for secondary regularization, is itself a low-pass filter. (See Fig. 1 of Stolz et al.[32]) For causal filtering, each is complex; as a consequence, $H * \tilde{H}^{-1}$ is poorly behaved. Figure 5 displays the moduli $|H|$, $|\tilde{H}^{-1}|$, and $|H * \tilde{H}^{-1}|$ obtained from the differential filter (Eq. 8) and $p$-th order deconvolution (Eq. 31) for selected values of $p$. It is clear that the product $|H * \tilde{H}^{-1}|$ converges as expected toward the identity operator as $p$ increases; however, convergence is slow, and for low-order deconvolution, conventional deconvolution actually increases energy in unresolved scales of motion. Moreover, as stated previously, for deconvolution methods with applications to LES/TLES, one wants the product $H * \tilde{H}^{-1}$ not to replicate the identity operator but to have the character of a high-order low-pass filter, so that large scales of motion are recovered faithfully even as small scales of motion are attenuated.

These difficulties can largely be circumvented by defining the approximate deconvolution in the standard way as

$$v_i = \sum_{k=0}^{p} c_k \bar{u}_i^{(k+1)} \tag{37}$$

but with coefficients $c_k$ optimized to give both $|H * \tilde{H}^{-1}|$ and $|I - H * \tilde{H}^{-1}|$ the following desirable properties:

1. $|H * \tilde{H}^{-1}(0)| = 1$
2. $|H * \tilde{H}^{-1}(\pi)| << 1$
3. $|H * \tilde{H}^{-1}| < 1$ for all $\Omega$
4. A minimal sum of absolute values of the low-order derivatives of $|H * \tilde{H}^{-1}|$ at the origin
5. $|I - H * \tilde{H}^{-1}| < 1$

The first constraint, imposed as strict equality, requires that the coefficients sum to unity; that is, $\sum_{j=0}^{p} c_k = 1$. The remaining constraints are "soft" in that they can be imposed in optimization packages via inequalities or minimization requests. The use of soft constraints prevents the system from being overconstrained whenever $p$ is small. For example, for $p = 3$, a set of coefficients found by optimization strategies is

$$\{c_0, c_1, c_2, c_3\} = \{0.99693, 0.503349, -0.684561, 0.184282\} \tag{38}$$

Figure 6 shows the moduli $|H|$, $|H^{-1}|$, $|H * \tilde{H}^{-1}|$ and $|I - H * \tilde{H}^{-1}|$ for the 3rd-order deconvolution coefficients immediately above and $r = 1$. Similarly Fig. 7 displays the same information for $r = 4$. Note that in either case $|H * \tilde{H}^{-1}|$ has desirable low-pass properties. Specifically, it has a flat plateau near the origin, so that large scales are recovered faithfully, yet small scales of motion are highly attenuated.

Figures. 6 and 7 also present the operator $|1 - H * \tilde{H}^{-1}|$ which is germane to secondary regularization. That the moduli lie between zero and one implies that all scales (except the mean) are attenuated by the secondary regularization operator, with extreme damping for the higher scales. The ideal shape for this operator is an inverted low-pass filter, with a flat plateau near the origin. Whereas, the operator is indeed inverted low-pass, it has non-zero slope near $\Omega = 0$, an undesirable trait. Thus, the TADM as presently configured may be more sensitive to the regularization parameter $\chi$ than is the ADM method, which, as mentioned previously, is reported to be relatively insensitive[32]. In summary, the coefficients $c_k$ presented above should be considered sub-optimal. Optimized temporal deconvolution will (hopefully) be the subject of a follow-on paper.

### E. Governing System

Recall that in the current time-filtered approach, the filter is imposed in differential form (Eq. 8). The governing equations thereby consist of evolution equations for the filtered velocities coupled to a set of evolution equations for additional filtered quantities as follows:

$$
\begin{aligned}
\frac{\partial \bar{u}_j}{\partial x_j} &= 0 \\
\frac{\partial \bar{u}_i}{\partial t} + \frac{\partial (\bar{u}_i \bar{u}_j)}{\partial x_j} &= -\frac{\partial \bar{p}}{\partial x_i} + \frac{1}{Re} \frac{\partial^2 \bar{u}_i}{\partial x_j \partial x_j} - \frac{\partial M_{ij}}{\partial x_j} \\
M_{ij} &= \overline{v_i v_j} - \bar{v}_i \bar{v}_j \\
v_i &= \sum_{k=0}^{p} c_k \bar{u}_i^{(k+1)} \\
\frac{\partial}{\partial t} \bar{u}_i^{(k+1)} &= \frac{\bar{u}_i^k - \bar{u}_i^{(k+1)}}{\Delta} \quad (1 \le k \le p) \\
\frac{\partial \bar{v}_i}{\partial t} &= \frac{v_i - \bar{v}_i}{\Delta} \\
\frac{\partial}{\partial t} (\overline{v_i v_j}) &= \frac{v_i v_j - \overline{v_i v_j}}{\Delta}
\end{aligned}
\tag{39}
$$

where the entire system is parameterized by the temporal filter-width $\Delta$. As was shown in Pruett et al.[27], the exact and modeled residual stresses vanish identically as $\Delta \longrightarrow 0$. Thus, as the filter width tends toward zero, the TFNSE tend smoothly toward the NSE, and TLES tends smoothly toward DNS.

The system above is presented without secondary regularization, which as mentioned previously, is a necessary form of artificial dissipation. The imposition of secondary regularization is simple; to the right-hand side of Eq. 39 expression 35 is appended. With secondary regularization, there are two arbitrary parameters, the deconvolution order $p$ and the dissipation parameter $\chi$. The filter width $\Delta$ is not considered arbitrary; it can and should be established on the basis of physical considerations, as discussed later.

At first inspection, it appears that the computational overhead for TLES is high, both in terms of storage and machine operations. In addition to the original storage required for the four primitive variables, storage locations are required for the nine (distinct) variables $\bar{v}_j$ and $\overline{v_i v_j}$, as well as for the $3p$ variables $\bar{u}_j^{(k)}$, $j = 2, ..., p+1$. Thus, for $p = 0$ and $p = 3$, for example, the total storage for TLES is about three times and seven times, respectively, that of a simulation without the model. However, if TLES permits significant grid coarsening relative to fully resolved DNS, then the net storage savings could be significant. For example, for $p = 3$, a TLES coarsened by a factor of four in each spatial dimension and time relative to DNS would necessitate only 10 percent of the memory required by the DNS. TLES is more benign with regard to computational effort. Although the governing system has grown from three evolution equations to $9 + 3p$ equations ($v_j$ do not involve evolution equations), the additional equations are linear and involve no spatial differentiation. Hence, even for $p = 3$, the computational cost of evaluating all additional filter equations remains less than that of evaluating the three momentum equations. Further reductions in computational overhead, for example, would be possible if one were willing to settle for an isotropic residual-stress model. No attempt to optimize either storage or computational effort has been yet undertaken, and it is likely that the TADM can be streamlined considerably.

## VI. REFERENCE DNS

For several reasons, plane-channel flow affords an ideal test case against which to benchmark present methodology. Channel flow involves wall effects, which are highly anisotropic, yet lends itself to fully spectral numerical methods, highly prized because of their accuracy and computational efficiency. Moreover, in its stationary turbulent state, channel flow is homogeneous in two of three spatial dimensions, which reduces the data output of post-processing. For these reasons, channel flow has been studied extensively[14–17,34], and a highly accurate data base is available (Moser et. al[17]). By convention, we will refer to this data base as KMM, as it originated with the work of Kim et al.[15] As a point of reference, Fig. 8 presents the streamwise velocity ($u_1$) profiles for the KMM cases of $Re_\tau = 180$ and $Re_\tau = 590$ vs. that of the laminar state, which is parabolic in the transverse coordinate. Here, $Re_\tau$ is the Reynolds number based upon the mean friction velocity $u_\tau$ (to be defined shortly). and channel half width. To ensure consistency of results, we have repeated the DNS of Moser et al. for nominal $Re_\tau = 180$.

### A. Numerical Method

The DNS is conducted by solving the NSE (that is, no residual-stress model) with the spectrally accurate channel-flow code TRANSIT of Gilbert and Kleiser[12]. The Navier-Stokes equations are solved in spectral space using Fourier expansions in the periodic streamwise ($x$) and transverse ($y$) directions and Chebyshev polynomial expansions in the wall-normal ($z$) direction. Collocation points are equally spaced in the periodic dimensions and are distributed at the Gauss-Lobatto points in the wall-normal direction. Nonlinear products are computed pseudospectrally by fast transform methods. An option exists in the code to run with dealiasing according to the 3/2 rule or without explicit dealiasing. Another option exists regarding the assumption of transverse symmetry; per-step computational efficiency is improved by a factor of two with symmetry enforced. Time advancement is semi-implicit and couples Crank-Nicolson splitting of diffusion terms with third-order low-storage Runge-Kutta time advancement of advection terms. A hallmark and innovation of TRANSIT is the enforcement of the divergence-free condition to machine (double) precision through an influence-matrix technique. The computational domain is a box of dimensions $L_1 = 2\pi/\alpha_1$, $L_2 = 2\pi/\alpha_2$, and $L_3 = 2$ in the streamwise, transverse, and wall-normal directions, respectively. TRANSIT, which performs temporal DNS, permits the computational box to convect at phase velocity CPH. All computations discussed herein, both DNS and TLES, were performed with CPH=0.0, for reasons explained subsequently.

For some simulations, the flow is initialized to a perturbed laminar state, for which the streamwise velocity profile is parabolic (Fig. 8) with centerline value unity; that is, $u(z) = 1 - z^2$. For others, to spare computational effort, the simulation is initialized to a nominally turbulent state. In either case, the flow is allowed to evolve through an initially transient period to stationarity, at which point statistical post-processing begins. Which of these initial conditions is exploited for a particular simulation will be reported in context. Without the enforcement of transverse symmetry, randomness in the initial conditions results in slightly asymmetric velocity and Reynolds-stress profiles. Rather than to enforce symmetry during the simulation, we prefer to allow asymmetry but to compute statistical quantities by averaging the upper and lower channel halves, which can be considered different realizations. Thus, the additional computation time per step is offset by the need for fewer time steps.

Channel-flow simulations are non-dimensionalized in several ways. To avoid confusion, we draw attention to three different methods for expressing the Reynolds number. In each case, $Re = U\delta/\nu$, where $U$ is the reference velocity, $\delta$ is the channel half width (assumed without loss of generality to be unity), and $\nu$ is the kinematic viscosity. The specifications differ in their reference velocities $U$. $Re_{\mathrm{lam}}$, $Re_{\mathrm{bulk}}$, and $Re_\tau$ result from using the laminar centerline velocity $U_{\mathrm{lam}}$, the laminar bulk velocity $U_{\mathrm{bulk}}$, and the friction velocity $u_\tau$, respectively, as the reference velocity, where $u_\tau = \sqrt{\nu \frac{\partial < u_1 >}{\partial z}}$. Without loss of generality, we presume $U_{\mathrm{lam}} = 1$, in which case $U_{\mathrm{bulk}} = 2/3$; hence, $Re_{\mathrm{bulk}} = 2/3 Re_{\mathrm{lam}}$. The nominal $Re_\tau = 180$ case of Moser et al. corresponds to $Re_{\mathrm{bulk}} = 2800$ ($Re_{\mathrm{lam}} = 4200$). The flow is driven either by a streamwise pressure gradient or by requiring the mass-flow rate to be constant. The latter option is preferred computationally, because the flow settles more quickly to stationarity (N. Adams, personal communication). Moreover, for this option, the mass-flow rate remains 4/3 at all times, as can be readily derived by integrating the laminar initial profile between -1 and +1 with $U_{\mathrm{lam}} = 1$. Knowing the mass-flow rate in advance is advantageous in ensuring consistency among competing scalings.

Finally, we note that $Re_\tau$ is the time mean of the instantaneous quantity $\tilde{Re}_\tau = \tilde{u}_\tau \delta/\nu$, where $\tilde{u}_\tau$ is the instantaneous friction velocity, defined as $\tilde{u}_\tau = \sqrt{\nu \frac{\partial < u_1 >_{x,y}}{\partial z}}$.

## B. DNS Test Cases

Parameter values for the DNS test cases are summarized below in Table I. Here $N_x$, $N_y$, and $N_z$ are the numbers of collocation points in the respective coordinate dimensions. Note that for TRANSIT, $Re_{\mathrm{lam}} = 3/2 Re_{\mathrm{bulk}}$ is a fixed input parameter, but that $\tilde{Re}_\tau$ is a time-dependent output result of the simulation, whose long-time mean is $Re_\tau$.

TABLE I: Parameter values for reference DNS cases.

| Case | $N_x \times N_y \times N_z$ | $\Delta t$ | $\alpha_1$ | $\alpha_2$ | $Re_{\text{bulk}}$ | $Re_\tau$ | dealiased? |
|---|---|---|---|---|---|---|---|
| KMM | $128 \times 128 \times 129$ | — | 0.5 | 1.5 | 2800 | 178.1 | yes |
| DNSa | $128 \times 128 \times 129$ | 0.01 | 0.5 | 1.5 | 2800 | 176.2 | yes |
| DNSb | $128 \times 128 \times 129$ | 0.01 | 0.5 | 1.5 | 2800 | $\approx 162$ | no |

### C. Results

To provide a well-documented reference flow against which to compare TLES results, we discuss the DNS results, with close attention to stationarity, homogeneity, and anisotropy, in addition to presentations of mean velocity profiles and mean Reynolds stresses. For brevity, we refer to simulations with resolution $128 \times 128 \times 129$ as having resolution $128^3$.

#### *1. Homogeneity*

In temporal DNS of plane channel flow, the flow is (by definition) periodic and homogeneous in the streamwise dimension. Channel flow is also periodic in the spanwise dimension; however, homogeneity must be established. Figure 9 displays $< u_1 >_{t,x} (y)$ at two (arbitrary) wall-normal stations: $z = 0$ and $z = .9988$. The spanwise variations are shown relative to their spanwise mean values. Temporal window averages are obtained for $\Delta = 50$ and $\Delta = 200$. As the window size increases the amplitude of the spanwise deviation about the mean appears to diminish, which suggests that the flow is homogeneous in $y$ for an appropriately long time scale (somewhat longer than present computational limitations allow). We now exploit homogeneity to reduce the turbulent statistics to functions of one dimension ($z$) by averaging spatially over wall-parallel planes.

#### *2. Stationarity*

Figure 10 displays the instantaneous and mean values of two turbulence statistics of interest: $Re_\tau$ and turbulent kinetic energy $k$ for the time interval $0 \leq t \leq 200$. These results suggest that the flow is stationary; however, rigorous confirmation of stationarity would require a time interval considerably longer than what practical computational limitations allow.

### *3. Aliasing Error Control*

An initial surprise was the effect of aliasing error upon the flow statistics. Cases DNSa and DNSb differ only in the parameter that invokes or bypasses aliasing error control. However, as shown in Fig. 11, their results differ by approximately 16 in $Re_\tau$. Moreover, such a difference in $Re_\tau$ induces noticeable differences in mean velocity profiles. The significant differences between the aliased and dealiased results suggest that spectral simulations at $Re_\tau = 180$ of $128^3$ resolution are adequately resolved but not highly resolved. Given that computational limitations typically force simulations to be conducted at marginal resolution, it is imperative that aliasing error be controlled explicitly.

For TRANSIT, dealiasing is performed unconventionally by increasing the resolution by a factor of 3/2 in each dimension prior to the transform to physical space, where nonlinear products are computed. Following the evaluation of nonlinear terms, resolution is returned to its nominal values by spectral truncation in Fourier space. This approach, which saves storage, is costly in another respect, namely that the per-step computational time nearly quadruples with explicit dealiasing. The necessity of controlling aliasing error also has connotations for TLES, which are addressed later.

### *4. Mean Profiles*

Figure 12 compares the mean streamwise velocity and its wall-normal derivative for the present simulation against that of the standard of Moser et al. The streamwise velocity profile is presented both in standard units and in wall units, $u_1^+$ [$= u_1/u_\tau$] vs. $z^+$ [$= zu_\tau/\nu$]. Whereas the presentation in standard units requires rescaling the KMM data, the presentation in wall units requires rescaling current results. That the results are virtually indistinguishable ensures not only that the two independently developed codes are giving consistent results, but also that the different scaling conventions have been interpreted in a mutually consistent manner.

### 5. *Reynolds Stresses and Anisotropy*

Figure 13 compares mean Reynolds stresses from the present simulation with the standard of Moser et al. for nominal $Re_\tau = 180$. The agreement is very good, which validates both the algorithm and the parameter settings.

The trace elements of the mean Reynolds-stress tensor afford a measure of anisotropy, which we take to be the ratio of twice the streamwise component to the sum of the remaining diagonal components, the value of which is presented in Fig. 14 as a function of wall-normal coordinate. For an isotropic flow, this ratio is identically one. As the figure shows, channel flow is highly anisotropic near the walls, being strongly dominated there by streamwise velocity fluctuations.

In Eq. (7.10) of Pope[22], the author presents a shear stress balance for turbulent channel flow. In dimensionless form with current scalings and (without loss of generality) $\rho = 1$, the total shear stress $\tau$ depends only on $z$ as follows:

$$\frac{\tau(z)}{u_\tau^2} = \frac{du_1^+}{dz} - \frac{\tau_{13}}{u_\tau^2} \tag{40}$$

where $\tau_{13} =< u_1' u_3' >$ is the (1,3) component of the Reynolds-stress tensor. Moreover, in Eq. (7.13), Pope shows the total stress profile to be linear. That is, the sum of viscous and Reynolds stresses across the channel is linear. Figure 15 confirms this relationship for case DNSa.

## VII. RESULTS OF TLES

The current section consists of three subsections. In the first, three coarse-grid simulations of channel flow at nominal $Re_\tau = 180$ are presented to establish a baseline for evaluating the effectiveness of TLES with the TADM, the results of which are presented in the second subsection for $Re_\tau = 180$. The final subsection presents TLES results of channel flow for nominal $Re_\tau = 590$. For each case, results are referenced to those of DNS at equivalent $Re_\tau$, as discussed in the previous section. All simulations were conducted with CPH=0.0, a necessity, because non-zero phase velocity produces a Doppler shift in the effective filter frequency[23] that interferes with the interpretation of some results.

### A. Baseline Cases

Parameter values for the baseline coarse-grid cases at nominal $Re_\tau = 180$ are presented in Table II below. For all cases $\alpha_1 = 0.5$, $\alpha_2 = 1.5$, and $Re_{\text{bulk}} = 2800$ ($Re_{\text{lam}} = 4200$), in accordance with the values for the KMM case of (nominal) $Re_\tau = 180$. Whenever temporal filtering is involvee, the filter-width ratio $r = 8$. The reader is reminded that, whereas $Re_{\text{bulk}}$ ($Re_{\text{lam}}$) is an input parameter, $\tilde{Re}_\tau$ and its mean $Re_\tau$ are output values. The baseline cases are designed not to assess the effectiveness of the TADM, but rather to establish coarse-grid reference simulations against which the method may be evaluated. For all baseline cases, the initial condition is derived from fine-grid DNS results, which are interpolated onto the coarser grid. As such, the initial condition induces transients and does not identically satisfy zero mass divergence. The latter is satisfied to machine (double) precision at the end of the initial time step; however, it takes quite some time for transients to settle. The baseline cases represent simulations with no model (BASEa) and simulations with a minimal model (BASEbc), namely, a temporal scale-similarity model (TSSM), which is the degenerate case of the TADM for $p = 0$[27]. The TSSM is the temporal analog of the Bardina model[4], which is known to be insufficiently dissipative. Cases BASEbc differ only in the de-aliasing option.

In Stolz et al.[32], the authors reported that, prior to the advent of the ADM, of all residual-stress models tested for channel flow, the most effective was no model whatsoever. This situation was improved substantially by the introduction of the ADM, which in our judgment, now represents the *de facto* state-of-the-art in residual-stress modeling, certainly, at least, for channel flow. Consequently, Table II also includes parameter data for Case ADM-180a of Stolz et al.[32], which we refer to as SAK180a. The baseline simulations and that of SAK represent a suite of coarse-grid simulations against which to evaluate TLES/TADM. More specifically, TLES/TADM should be considered a moderately effective methodology if it improves substantially upon the "no model" case (BASEa), and very effective if it produces results roughly equivalent in accuracy to the standard (spatial) ADM method at commensurate resolution.

TABLE II: Parameter values for baseline coarse-grid simulatons.

| Case | $N_x \times N_y \times N_z$ | $\Delta t$ | $Re_{\text{bulk}}$ | $Re_\tau$ | dealiased? | model | $(r, p)$ |
|---|---|---|---|---|---|---|---|
| BASEa | $32 \times 32 \times 33$ | 0.04 | 2800 | 203 | yes | none | NA |
| BASEb | $32 \times 32 \times 33$ | 0.04 | 2800 | 182 | no | TSSM | (8,0) |
| BASEc | $32 \times 32 \times 33$ | 0.04 | 2800 | 203 | yes | TSSM | (8,0) |
| SAK180a | $32 \times 32 \times 33$ | — | 2800 | 173 | yes | ADM | NA |

### 1. *Case BASEa: No Residual-Stress Model; with Dealiasing*

Figure 16 displays computed $Re_\tau$ and turbulent kinetic energy $k$ for Case BASEa. This is also referred to as the "no-model" TLES, which is essentially coarse-grid DNS with dealiasing. The figure suggests that the flow is stationary by $t = 100$; consequently mean quantities presented below are computed by temporal averages taken over the interval $100 \leq t \leq 500$, as shown by the length of the horizontal line in Fig. 16 and subsequent figures. As discussed previously, mean data are computed by also averaging over homogeneous dimensions and exploiting symmetry.

Figure 17 presents the mean streamwise velocity and its wall-normal derivative vs. wall-normal coordinate $z$ for Case BASEa. Although the "no model" simulation appears to produce a nearly correct mean velocity according to Fig. 17(a), the slope of the velocity profile at the wall is approximately 30 percent in error, as indicated in Fig. 17(b)-(c). The error in wall velocity gradient results in $Re_\tau = 203.2$ for Case BASEa vs. $Re_\tau = 178.1$ for the DNS. Figure 17(c) presents the same information as Fig. 17(a), except expressed in wall units. More precisely, In Fig. 17(c), each profile is scaled according to the relevant calculated friction velocity $u_\tau = Re_\tau / Re_{\text{lam}}$; that is, according to $Re_\tau = 178.1$ for DNS and $Re_\tau = 203.2$ for BASEa. This convention has the effect of shifting the origin so that profiles match at the wall but deviate due to accumulated error away from the wall.

Figure 18 presents the four principal components of the Reynolds-stress tensor for Case BASEa, relative to the Reynolds stresses of the reference DNS of KMM. In Stolz et al.[32], a precedent was established for displaying trace elements of the Reynolds-stress tensor as fluctuation velocities $R_{ii}^{1/2}$. We adopt the same convention in Fig. 18 and subsequently. Relative to DNS, the "no model" case over-predicts all components of $\tau_{ij}$, with the (2,2) component some 60 percent in error. Here, to compare Reynolds stresses in absolute terms, both the DNS and BASEa values have been scaled by the same reference velocity, namely $u_\tau$ of the DNS. The customary rescaling of Reynolds stresses by the actual $u_\tau$ (in this Case $u_\tau = Re_\tau/Re_{\text{lam}} = 203.2/4200$) gives the appearance of a better fit of the model to the DNS reference data, but, in our view, is misleading because it masks the effects of under- or over-estimating the wall stress $\tau_w$.

### *2. Case BASEb: TSSM Residual-Stress Model without Dealiasing*

Figures 19, 20, and 21 display the same information as in the previous case, but for Case BASEb. Figure 19 suggests that the flow is somewhat transient until $t \approx 200$, but is essentially stationary for $t > 200$. Average $Re_\tau$ for $200 \leq t \leq 500$ is 181.9. To approximate $k(t)$ for Case BASEb, we have exploited Eq. 25, albeit with modeled residual stress $M_{ii}$ in lieu of $R_{ii}$.

For Fig. 21, Reynolds stresses for Case BASEb are approximated as the sum of the resolved-scale Reynolds stress and the mean modeled residual stress, according to Eq. 21 with $M_{ij}$ replacing $R_{ij}$. The contribution of the modeled residual stress to the total Reynolds stress is also presented. Reynolds stresses are considerably in error near the walls, where $\tau_{11}$ is under-predicted and $\tau_{22}$ and $\tau_{33}$ are over-predicted. In particular, the (2,2) component is over-predicted by about 60 percent. Errors in Reynolds stress induce considerable mean-flow error, as shown in Fig. 20.

From these results and the results of the DNS of the previous section, we conclude that dealiasing is essential.

### *3. Case BASEc: TSSM Residual-Stress Model; with Dealiasing*

Figures 22, 23, and 24 display the same information as previously, but for Case BASEc, for which the model is the TSSM. In general, it appears that the $p = 0$ case performs no better and no worse than the no-model case. That all three coarse-grid baseline test cases predict Reynolds stresses and turbulent kinetic energy to be in excess of that of the DNS (Fig. 10) confirms that the baseline models are insufficiently dissipative as expected.

## B. TLES with Full TADM for Nominal $Re_\tau = 180$

Here we present results of TLES with a full TADM for nominal $Re_\tau = 180$; that is, the residual-stress "model" incorporates both high-order deconvolution and secondary regularization. For each case the deconvolution is of order $p = 3$ with "tuned" coefficients, as discussed in Section V. The parameters of the test cases are given in Table III below. As for the results of the previous section, $\alpha_1 = 0.5$ and $\alpha_2 = 1.5$ for all test cases, and $Re_{\text{bulk}} = 2800$ ($Re_{\text{lam}} = 4200$), for congruence with the results of KMM at $Re_\tau = 180$. The filter-width ratio $r$ and regularization coefficient $\chi$ are provided in the last column of the table. Unlike the baseline cases established above, the initial condition for all TLES cases at $Re_\tau = 180$ is that of a randomly perturbed laminar channel flow.

TABLE III: Parameter values for TLES cases.

| Case | $N_x \times N_y \times N_z$ | $\Delta t$ | $Re_{\text{bulk}}$ | $Re_\tau$ | $(r;\chi)$ |
|---|---|---|---|---|---|
| TLES180a | $32 \times 32 \times 33$ | 0.04 | 2800 | 172.5 | (08,0.5) |
| TLES180b | $32 \times 32 \times 33$ | 0.04 | 2800 | 179.2 | (08,0.3) |
| TLES180c | $32 \times 32 \times 33$ | 0.04 | 2800 | 184.7 | (08,0.2) |
| TLES180d | $32 \times 32 \times 33$ | 0.04 | 2800 | 162.0 | (16,0.1) |

For brevity we present graphically the results of Cases TLESb, TLESc, and TLESd only (Figs. 25-34). All TLES results except TLESd show marked improvement relative to the corresponding results of the coarse-grid baseline Cases BASEa-c. In particular, the TLES meanflow profiles very nearly match those of the DNS. Secondary regularization provides an adequate sink for energy at marginally resolved scales, as evidenced by decreases in turbulent kinetic energy $k$ and $Re_\tau$ relative to the baseline cases. At present, the value of the regularization parameter $\chi$ is arbitrary, and an appropriate value is found by numerical experimentation (as is also true for the conventional ADM). For fixed $r$, variations of $\chi$ by a factor of 2.5 do not change the results dramatically, as can be seen by comparing the $\chi = 0.5$ and $\chi = 0.2$ cases for $r = 8$. The insensitivity to $\chi$ of the conventional (spatial) ADM is discussed in Stolz et al.[32]. As expected, the current TADM appears to be more sensitive to $\chi$ than the ADM. Acceptable results, however, are obtained for a range of values of $\chi$. For Case TLESd, the level of dissipation imposed by the large filter width and the secondary regularization is quite high, and it is clear that the combination is overly dissipative.

In contrast to the ADM of[32], for which the filter width is fixed, the current TADM is parameterized by the filter-width ratio $r$. As implied in Figs. 6 and 7, the secondary regularization operator becomes more dissipative with increasing $r$ at roughly a linear rate. Improvement of the secondary regularization operator for the TADM will be the subject of follow-on research.

Figure 28 below establishes for Case TLESc that TLES of channel flow follows a stress balance analogous to that shown in Fig. 15 for Case DNSa, except that there is an additional contribution to the total mean shear stress through the mean modeled residual stress. Here, the velocity scale is the computed (rather than nominal) value of $u_\tau = 179.2/4200$. Low-level oscillations in the linear profile suggest, however, that $32^3$ spatial resolution is marginal.

In contrast to the baseline cases, all TLES cases for $Re_\tau = 180$ are initialized to a laminar state subject to random perturbations. Thus, the computation proceeds from perturbed laminar flow, through transition, to a stationary turbulent state. Transitional flow is characterized by a strong spike in turbulent kinetic energy $k$, as evidenced in Figs. 25, 29, and 32. In the initial stages of transition, the flow is primarily two-dimensional. Late-stage transition is characterized by loss of two-dimensionality and the prevalence of three-dimensional structures. In the final breakdown stage, $k$ "relaxes" toward a lower value characteristic of a fully turbulent state.

In general, it is difficult for LES to properly treat transitional flow. On the one hand, the standard Smagorinsky model is excessively dissipative and typically inhibits transition altogther. On the other hand less dissipative methods tend to blow up during the spike in $k$ associated with transition. That TLES, properly tuned, can allow for transition, yet settle into a statistically nearly-correct turbulent state, is noteworthy.

### C. TLES with Full TADM for Nominal $Re_\tau = 590$

Channel flow at nominal $Re_\tau = 180$ is generally considered "barely turbulent." Consequently, it is highly desirable to validate TLES at much higher Reynolds number, for which we consider nominal $Re_\tau = 590$. Table IV summarizes the parameter values of the present TLES relative to those of the reference DNS of KMM for nominal $Re_\tau = 590$. The table also presents parameter data regarding channel-flow DNS and LES conducted at the same nominal Reynolds number by Stolz, Adams, and Kleiser (SAK)[32]. More precisely, all simulations were conducted at $Re_{\text{bulk}} = 10935$ ($Re_{\text{lam}} = 16400$) with box parameters $\alpha_1 = 1$ and $\alpha_2 = 2$. For this parameter set, KMM obtained $Re_\tau = 587$. Independent replication of the DNS by SAK, who used TRANSIT and the same spatial resolution as KMM, resulted in $Re_\tau = 586$. Thus, very high confidence exists in the reference DNS data.

Course-grid simulation with no model (other than explicit dealiasing) by SAK yielded $Re_\tau = 633$, an error by about eight percent, which corresponds to an overshoot of approximately 16 percent in the mean wall-normal derivative of the streamwise velocity at the wall. In constrast, SAK obtained $Re_\tau = 574$ and $Re_\tau = 587$ for their LES cases 590a and 590b, errors of just over two percent and zero percent, respectively. Cases SAK590a and SAK590b each exploit the standard (spatial) ADM and differ only in resolution.

TABLE IV: Parameter values for TLES and reference simulations at nominal $Re_\tau = 590$.

| Case | $N_x \times N_y \times N_z$ | $Re_\tau$ | model |
|---|---|---|---|
| DNS (KMM) | 384 × 384 × 257 | 587 | NA |
| DNS (SAK) | 384 × 384 × 257 | 586 | NA |
| LES (SAK) | 48 × 64 × 65 | 633 | none |
| LES (SAK590a) | 48 × 64 × 65 | 574 | ADM |
| LES (SAK590b) | 72 × 96 × 97 | 587 | ADM |
| TLES590 | 48 × 64 × 65 | 564 | TADM |

We consider TLES at the same resolution as SAK590a with the tuned ($p = 3$) TADM coefficients of Eq. 38 and parameter values $\Delta t = 0.04$, $r = 8$, and $\chi = 0.3$. Figure 35 presents the evolution of instantaneous $\tilde{Re}_\tau$ and $\bar{k}$ for Case TLES590, from a nominally turbulent initial state. Figures 36 and 37 present the mean streamwise velocity (and its wall-normal derivative) and the Reynolds-stress distributions, respectively, for Case TLES590. It is fair to say that TLES with the TADM performs nearly as well as the standard ADM at commensurate resolution. It is worth noting that, in contrast to the TLES cases at nominal $Re_\tau = 180$, no numerical experimentation was performed to optimize parameters. That is, optimal values obtained for $Re_\tau = 180$ were simply translated directly to $Re_\tau = 590$. However, at this Reynolds number and with these parameter values, the simulation had insufficient dissipation to survive transition. Mean quantities are computed by averaging over $500 \leq t \leq 2000$, following the settling of initial transients.

## VIII. DISCUSSION

The computational savings of TLES relative to DNS are significant. For example, the $32^3$ TLES cases at nominal $Re_\tau = 180$ ran to completion in approximately one one-hundredth of the time required for DNS at a resolution of $128^3$. The speedup comes not only because of grid coarsening by a factor of four in each spatial dimension, but also by similar coarsening in time, for an aggregate workload reduction factor of $4^4 = 256$. However, at commensurate resolutions, the computational overhead of TLES relative to DNS is approximately a factor of two, for a net gain in efficiency of roughly $10^2$. At $Re_\tau = 590$, the computational gains of TLES are even more significant, as can be seen by comparing resolutions for DNS and TLES in Table IV.

It is useful to establish a practical rule of thumb in regard to the choice of $r$ (which effectively reduces the number of model parameters). One approach is to consider the ratio of the filter width $\Delta$ to the temporal integral scale $\bar{\tau}$, a scale characteristic of the turnover time of the largest eddies. Figure 38 presents selected mid-plane ($z = 0$) time traces of the velocity components from Case TLES590. Associated with any time series is its autocorrelation function $\rho(s)$ (Fig. 39), which in general, is given by by

$$\rho(s) = \frac{< u(t)u(t+s) >}{< u(t)^2 >} \tag{41}$$

Several measures of the integral scale $\bar{\tau}$ can be extracted from the autocorrelation function. The favored is

$$\bar{\tau} = \int_0^\infty \rho(s) ds \tag{42}$$

provided that the integral converges. If the integral does not converge, it is sometimes useful to let the first zero crossing of the autocorrelation function represent $\bar{\tau}$. Figure 39 presents a composite autocorrelation function derived by averaging the $N_x * N_y$ individual autocorrelations, each associated with a time series of $\bar{u}_j$ recorded at one of the mid-plane grid points. A time-series is displayed for $\bar{u}_1$ in Fig. 38. The autocorrelation functions of the velocities are quasi-periodic in time, as is to be expected. Although strict temporal periodicity is destroyed by the nonlinearity of the governing system, enforced spatial periodicity nonetheless induces temporal quasi-periodicity. Because of the large mean streamwise component, Eq. 42 fails to converge for $\bar{u}_1$. Consequently, we use the first zero crossings from the autocorrelations of $\bar{u}_2$ and $\bar{u}_3$ as representative of the integral scale; thus, $\bar{\tau} \approx 2$. The temporal resolution of Case TLES590 is such that there are approximately 50 time steps per large-eddy turnover. Consequently, $r = 8$ translates to a filter width of approximately 16 percent of the integral scale.

This suggests a possible overarching rule of thumb. TLES should behave as RANS when the filter width $\Delta$ is many times the integral scale (provided the SFS model is adequate at large $\Delta$). For $\Delta$ a sizable fraction of $\bar{\tau}$, say 50 percent, then TLES should effectively act as unsteady RANS (URANS). At the other extreme, for $\Delta$ quite small, say 1-2 percent of $\bar{\tau}$, TLES is virtually equivalent to DNS. Finally, for $\Delta$ values that range from, say, 5-25 percent of $\bar{\tau}$, TLES is the temporal analog of LES.

Equivalently, the distinctions among DNS, TLES, URANS, and RANS, can be drawn based upon the relative contributions of the residual stress to the Reynolds stress. As discussed in Section IV for RANS, the residual stress contributes 100 percent to the Reynolds stress. For DNS, the residual stress vanishes, and thus contributes nothing to the Reynolds stress. Between these extremes lie TLES and URANS. We would suggest that contributions of 5-50 percent of the residual stress to the Reynolds stress define TLES, and contributions greater than, say, 50 percent define URANS. These domain boundaries are admittedly arbitrary and are offered simply as talking points.

Finally, a few comments regarding the present SFS model are in order. There are two components to the model: the residual-stress model and secondary regularization. Experience to date suggests that the temporal residual-stress model is more than adequate. Deconvolution orders of 2, 3, and 5 have been examined, as have a variety of deconvolution coefficients and filter widths. In all cases the instantaneous and mean residual stresses are well-defined, with mean components that have qualitatively correct profiles. In sum, temporal deconvolution appears to admit a family of robust residual-stress models.

In contrast, temporal secondary regularization remains problematic, apparently due to the phase lag associated with causal filtering. As artificial damping (secondary regularization) is an essential component of the present model (or of any generalized similarity model), the issue requires further study and is the subject of an addendum to this report entitled "Optimized Temporal Deconvolution."

## IX. CONCLUSIONS AND FUTURE WORK

The present paper establishes temporal LES (TLES) as a viable alternative to conventional (spatial) LES. The methodology exploits a causal time-domain filter expressed in differential form, which yields a governing system of equations explicitly parameterized in terms of the temporal filter width $\Delta$. Sub-filter scales (SFS) are approximated by a temporal variant (TADM) of the approximate deconvolution model (ADM) of Stoltz and Adams[31]. The method is demonstrated by simulating plane-channel flows at $Re_\tau = 180$ and $Re_\tau = 590$. Results are compared against the benchmark channel-flow results of Kim et al.[17], obtained by well-resolved DNS with spectral methods.

Although there is likely considerable room for improvement in the current TADM, present results of TLES/TADM are nearly as good for channel flow as those obtained by LES/ADM and reported in Stolz et al.[32] (for commensurate resolution).

TLES enjoys some conceptual and practical advantages, which could make it the method of choice in certain applications. First, through the parameter $\Delta$, TLES provides a formal link among DNS, URANS, and RANS methodologies. Second, whereas spatial filtering is problematic for unstructured grids because of wide variations in grid size, temporal filtering, particularly in differential form, is independent of spatial grid resolution. Finally, present methodology provides direct means for comparing results of TLES with DNS or experiment, obviating the need for *a posteriori* analyses.

### Acknowledgments

The author is grateful to Prof. L. Kleiser of the Institute for Fluid Dynamics at ETH Zurich for permission to use the channel-flow simulation code (TRANSIT) of Gilbert and Kleiser and to R. Moser of the University of Illinois Urbana-Champaign for providing channel-flow reference data. The author is indebted to P. Schlatter of ETH for his expertise in channel-flow simulation, in general, and TRANSIT, in particular, and his patience in the face of numerous questions. The author also benefitted greatly from stimulating discussions with N. Adams of the Technical University of Dresden, with U. Rist, M. Kloker, O. Marxen and G. Bonfigli of the Institute for Aerodynamics and Gasdynamics at the University of Stuttgart, with W. Thacker of St. Louis Univeristy, and with S. Tieszen of Sandia Labora-

tories. Finally, he is grateful to J. Morrison of NASA Langley Research Center for helpful suggestions regarding computational platforms, compilers, and their relative efficiencies.

---

[1] N. A. Adams, "The use of LES subgrid-scale models for shock capturing," International Journal for Numerical Methods Fluids **39**, 783 (2002).

[2] N. A. Adams and S. Stolz, "Deconvolution methods for subgrid-scale approximation in LES," in *Modern Simulation Strategies for Turbulent Flows*, ed. B. J. Geurts, R. T. Edwards Publishing, 21 (2001).

[3] A. A. Aldama, *Filtering Techniques for Turbulent Flow Simulation*, Springer-Verlag, New York (1990).

[4] J. Bardina, J. H. Ferziger, and W. C. Reynolds, "Improved subgrid-scale models for large eddy simulation," AIAA Paper No. 80-1357 (1980).

[5] G. A. Blaisdell, "Computation of discrete filters and differential operators for large-eddy simulation," *Advances in DNS/LES*, C. Liu and Z. Liu (eds.), Greyden Press, Columbus, OH, 333 (1997).

[6] Y. M. Dakhoul and K. W. Bedford, "Improved averaging method for turbulent flow simulation. Part I: Theoretical development and application to Burgers' transport equation," International Journal for Numerical Methods in Fluids bf 6, 49 (1986).

[7] J. A. Domaradzki and E. M. Saiki, "A subgrid-scale model based on the Estimation of Unresolved scales of turbulence," Phys. Fluids A **9**, 2148 (1997).

[8] M. Germano, U. Piomelli, P. Moin, and W. H. Cabot, "A dynamic subgrid-scale eddy viscosity model," Phys. Fluids A **3**, 1760 (1991).

[9] M. Germano, "From RANS to DNS: Toward a bridging model," *Direct and Large-Eddy Simulation-III*, P. R. Voke, N. D. Sandham, and L. Kleiser (eds.), Kluwer, 225 (1999).

[10] M. Germano, "LES overview," in *DNS/LES Progress and Challenges*, C. Liu, L. Sakell, and T. Beutner (eds.), Greyden Press, Columbus, OH, 1 (2001).

[11] B. Geurts, "Inverse modeling for large-eddy simulations," Phys. Fluids **9**, 2148 (1997).

[12] N. Gilbert and L. Kleiser, "Near-wall phenomena in transition to turbulence," in *Near-Wall Turbulence* eds. S. J. Kline and N. H. Afgan, 7, Hemisphere (1990).

[13] J. Gullbrand, "Grid-independent large-eddy simulation in turbulent channel flow using three-

dimensional explicit filtering," *Center for Turbulence Research Annual Research Briefs*, 167 (2002).

[14] P. Moin and J. Kim, "Numerical investigation of turbulent channel flow," J. Fluid Mech **118**, 341 (1982).

[15] J. Kim, P. Moin, and R. Moser, "Turbulence statistics in fully developed channel flow at low Reynolds number," J. Fluid Mech **177**, 133 (1987).

[16] N. N. Mansour, J. Kim, and P. Moin, "Reynolds-stress and dissipation-rate budgets in a turbulent channel flow," J. Fluid Mech **194**, 15 (1988).

[17] R. D. Moser, J. Kim, N. N. Mansour, "Direct numerical simulation of turbulent channel flow up to $Re_\tau = 590$," Phys. Fluids **11**, 943 (1999).

[18] A. Leonard, "Energy cascade in large-eddy simulations of turbulent flows," Adv. Geophys. **18A**, 237 (1974).

[19] S. Liu, C. Meneveau, and J. Katz, "On the properties of similarity subgrid-scale models as deduced from measurements in a turbulent jet," *J. Fluid Mech.* **275**, 83 (1994).

[20] C. Meneveau, T. S. Lund, and W. H. Cabot, "A Lagrangian dynamic subgrid-scale model of turbulence," J. Fluid Mech., **319**, 353 (1996).

[21] U. Piomelli, P. Moin, and J. H. Ferziger, "Model consistency in large-eddy simulation of turbulent channel flow," Phys. Fluids A **31**, 1884 (1988).

[22] S. B. Pope, *Turbulent Flows*, Cambridge University Press (2000).

[23] C. D. Pruett, "On Eulerian time-domain filtering for spatial large-eddy simulation," AIAA J. **38**, 1634 (2000).

[24] C. D. Pruett and N. A. Adams, "*A priori* analyses of three subgrid-scale models for one-parameter families of filters," Phys. Fluids A **12**, 1133 (2000).

[25] C. D. Pruett, N. A. Adams, and J. S. Sochacki, "On Taylor-series expansions of residual stress," Phys. Fluids **13**, 2578 (2001).

[26] C. D. Pruett, "Toward the de-mystification of LES," *DNS/LES Progress and Challenges*, C. Liu, L. Sakell, and T. Beutner (eds.), Greyden Press, Columbus, OH, 247 (2001).

[27] C. D. Pruett, T. B. Gatski, C. E. Grosch, and W. D. Thacker, "The temporally filtered Navier-Stokes equations: Properties of the residual stress," Phys. Fluids **15**, 2127 (2003).

[28] N. D. Sandham and L. Kleiser, "The late stages of transition to turbulence in channel flow," J. Fluid Mech. **245**, 319 (1992).

[29] K. B. Shah and J. Ferziger, "A new non-eddy viscosity subgrid-scale model and its application to channel flow," in *CTR Annual Research Briefs 1995*, Center for Turbulence Research, Stanford University and NASA Ames Research Center, Stanford, California (1995).

[30] G. D. Stefano and O. V. Vasilyev, "A study of the effect of smooth filtering in LES," *DNS/LES Progress and Challenges*, C. Liu, L. Sakell, and T. Beutner (eds.), Greyden Press, Columbus, OH, 247 (2001).

[31] S. Stolz and N. A. Adams, "An approximate deconvolution procedure for large-eddy simulation," Phys. Fluids A **11**, 1699 (1999).

[32] S. Stolz, N. A. Adams, and L. Kleiser, "An approximate deconvolution model for large-eddy simulations with application to incompressible wall-bounded flows," Phys. Fluids **13**, 997 (2001).

[33] S. Stolz, N. A. Adams, and L. Kleiser, "The approximate deconvolution model for large-eddy simulations of compressible flows and its application to shock-turbulent-boundary-layer interaction," Phys. Fluids **13**, 2985 (2001).

[34] R. D. Strum and D. E. Kirk, *First Principles of Discrete Systems and Digital Signal Processing*, Addison-Wesley, New York (1988).

[35] O. V. Vasilyev, T. S. Lund, and P. Moin, "A general class of commutative filters for LES in complex geometries," J. Comput. Phys. **141**, 82 (1998).

## Figures

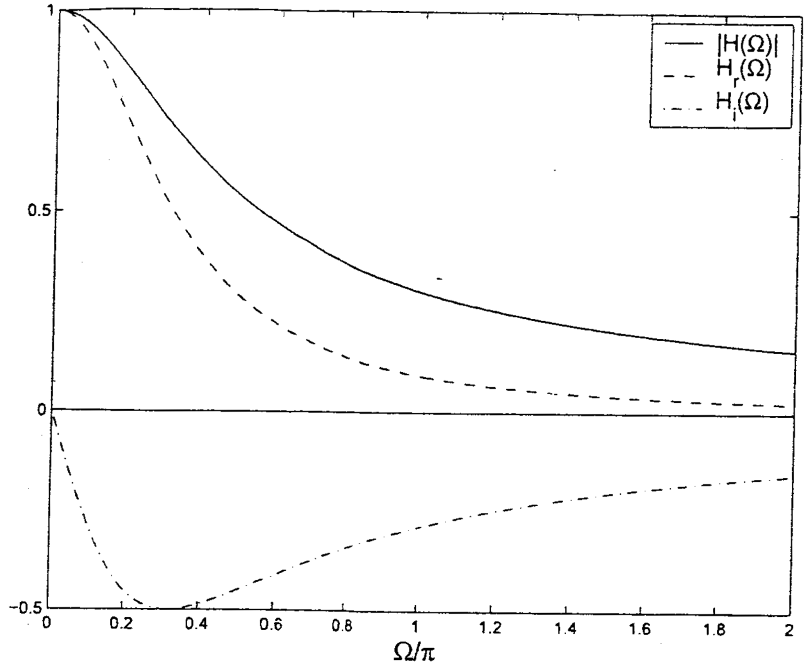

FIG. 1: Modulus and real and imaginary parts of transfer function of continuous causal exponential filter.

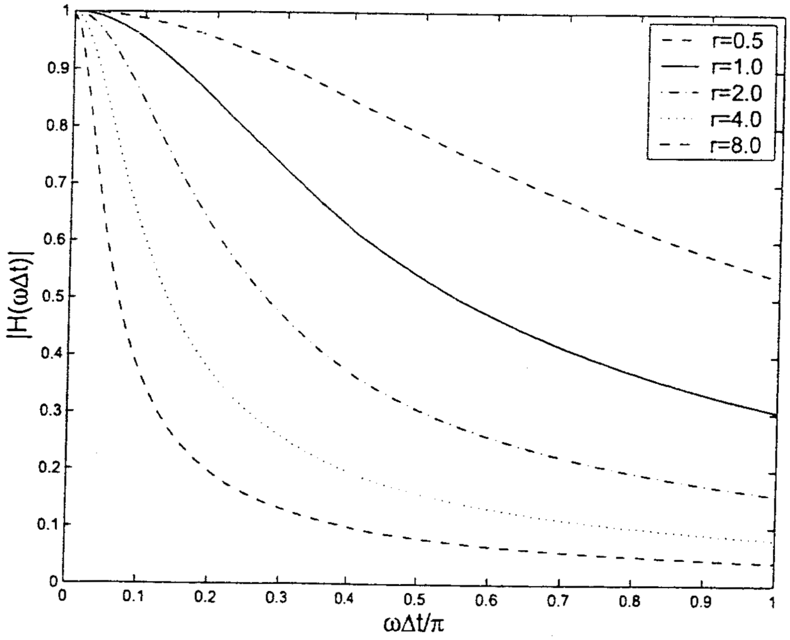

FIG. 2: Modulus of transfer function of parameterized exponential filter as a function of filter-width ratio.

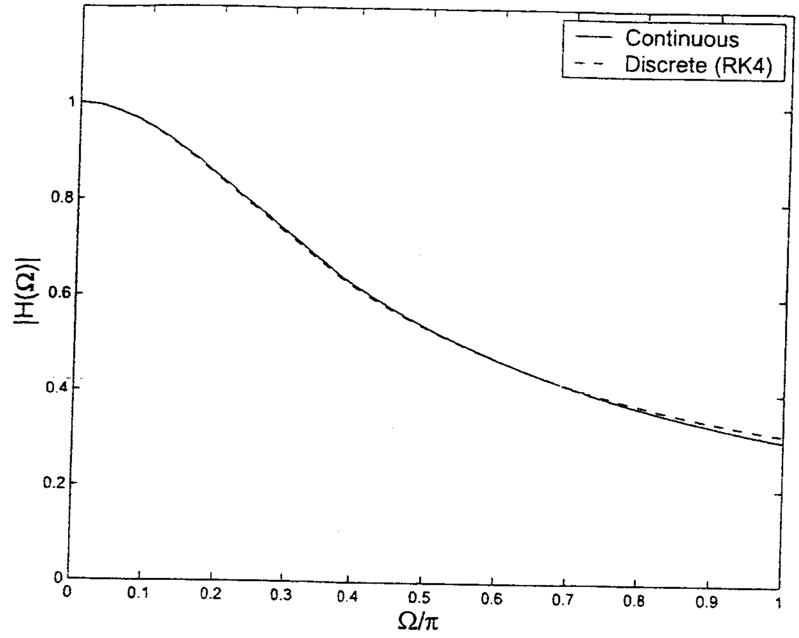

FIG. 3: Transfer functions of continuous and high-order discrete exponential filters.

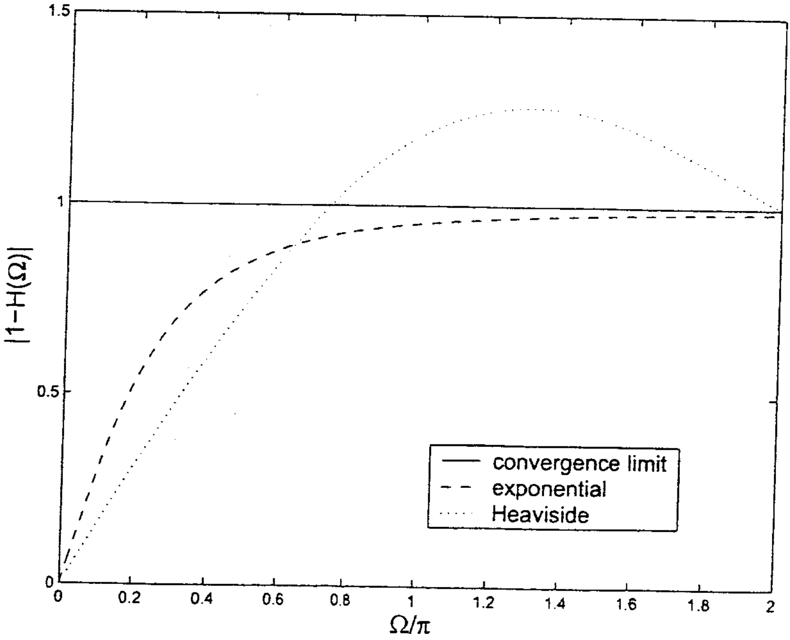

FIG. 4: Quantity $|1 - H|$, which determines convergence of Eq. 28 for exponential and Heaviside filters showing that Heaviside filter is not suitable for deconvolution.

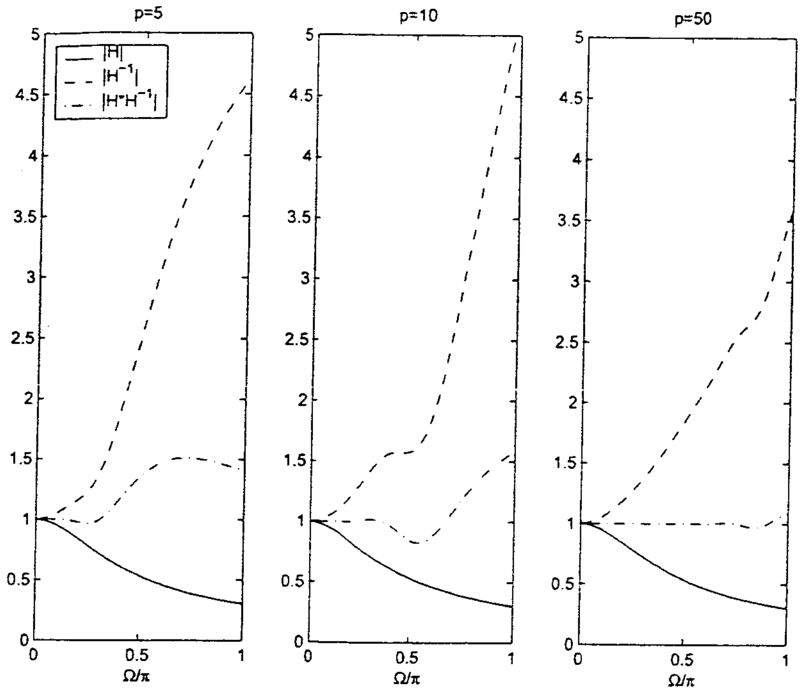

FIG. 5: Moduli of transfer function of exponential filter ($|H|$), its approximate inverse ($|\tilde{H}^{-1}|$), and their product ($|H * \tilde{H}^{-1}|$), for selected deconvolution orders $p$.

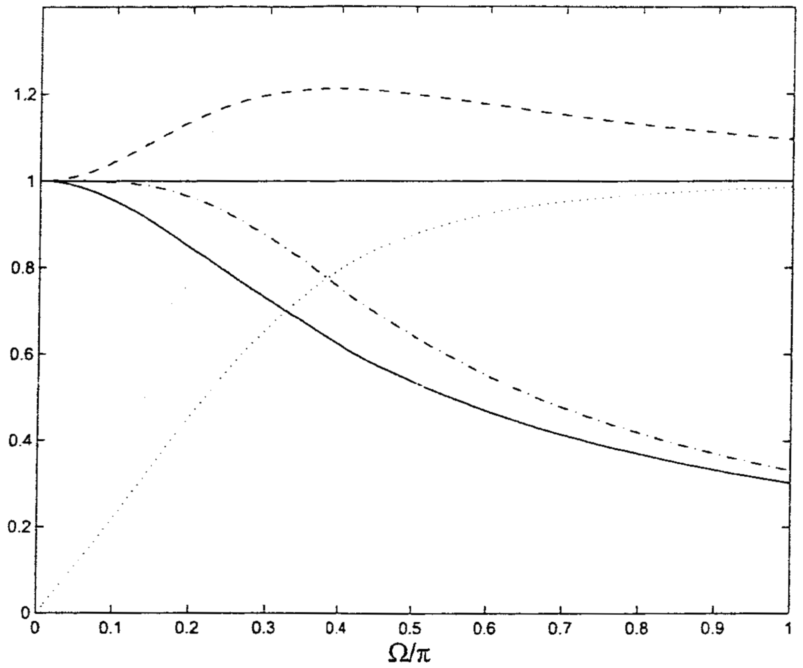

FIG. 6: Moduli of transfer function of exponential filter ($|H|$), its approximate inverse ($|\tilde{H}^{-1}|$), their product ($|H * \tilde{H}^{-1}|$), and secondary regularization operator ($|1 - H * \tilde{H}^{-1}|$) for tuned deconvolution of order $p = 3$ and filter-width ratio $r = 1$.

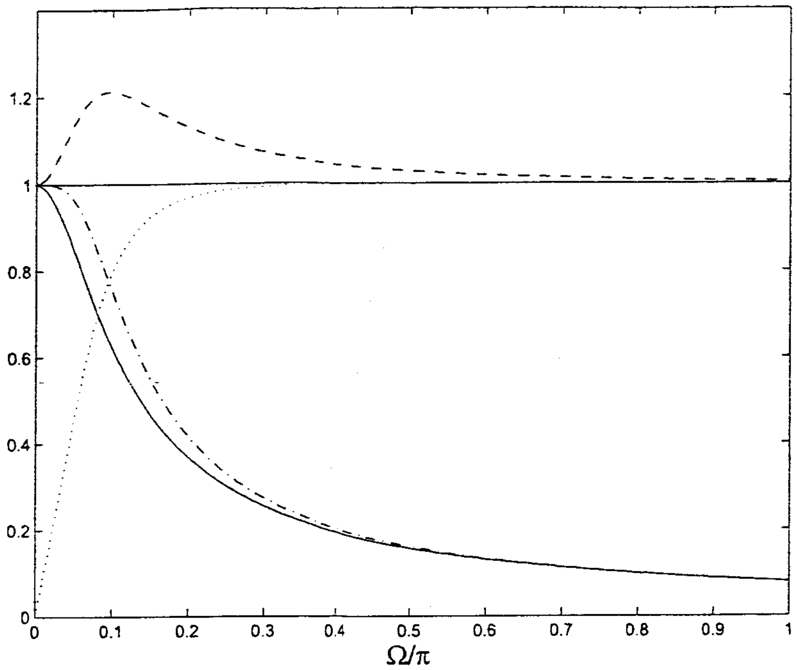

FIG. 7: Moduli of transfer function of exponential filter ($|H|$), its approximate inverse ($|\tilde{H}^{-1}|$), their product ($|H*\tilde{H}^{-1}|$), and secondary regularization operator ($|1-H*\tilde{H}^{-1}|$) for tuned deconvolution of order $p=3$ and filter-width ratio $r=4$.

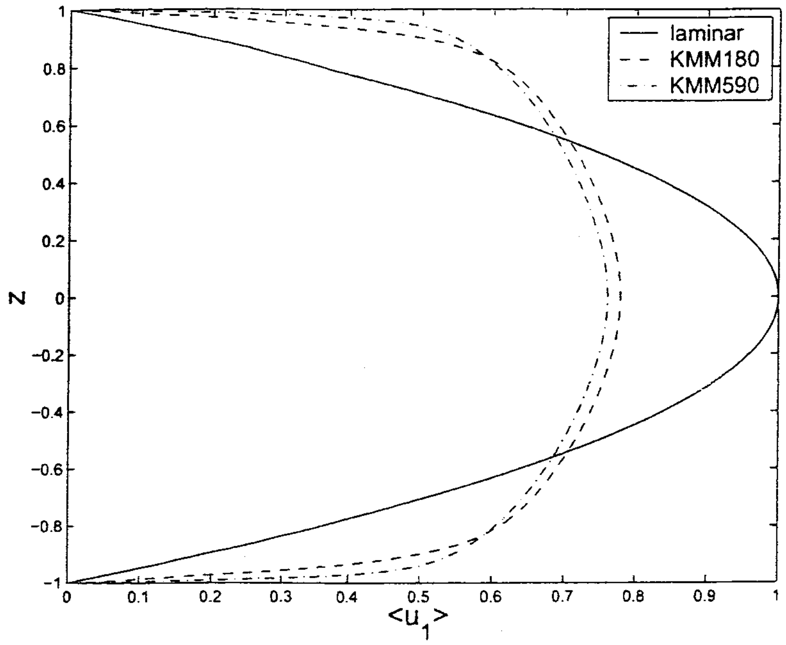

FIG. 8: Mean streamwise velocity profiles of KMM vs. parabolic profile of laminar state. (KMM data are replicated symmetrically about centerline for clarity.)

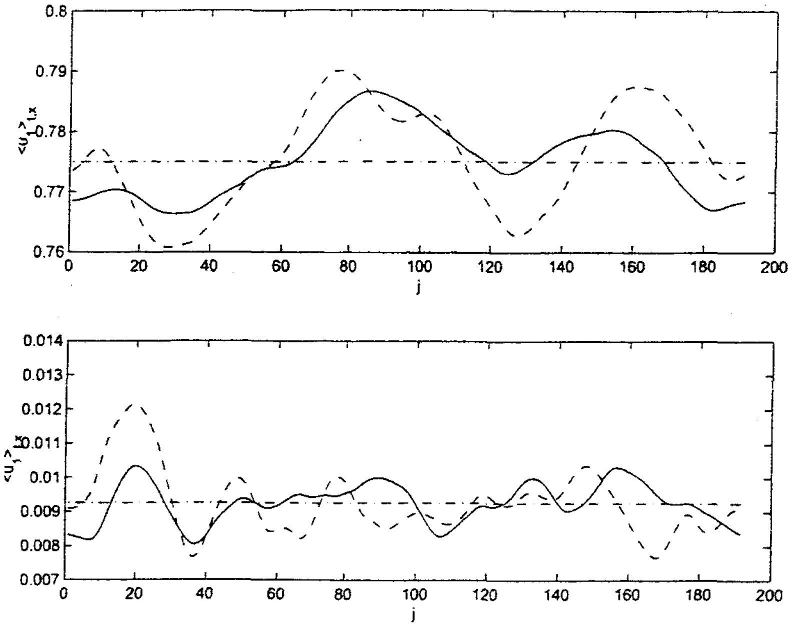

FIG. 9: Spanwise variation in average streamwise velocity $< u_1 >_{t,x} (y)$, for temporal windows of $\Delta = 50$ and $\Delta = 200$. Amplitude of spanwise variation diminishes with increasing window size, suggesting spanwise homogeneity on a sufficiently large time scale. LEGEND: solid line ($\Delta = 200$); dashed line ($\Delta = 50$); dashed-dotted line (mean). Upper figure: $z = 0.0$. Lower figure: $z = 0.9988$.

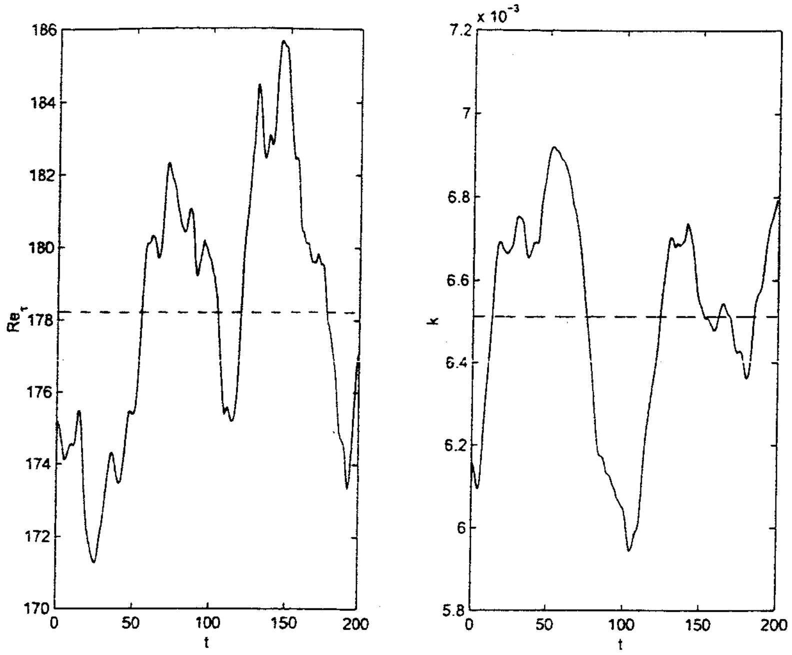

FIG. 10: Lower-wall $Re_\tau$ and turbulent kinetic energy $k$ vs. time for Case DNSa. LEGEND: solid line (instantaneous); dashed line (mean).

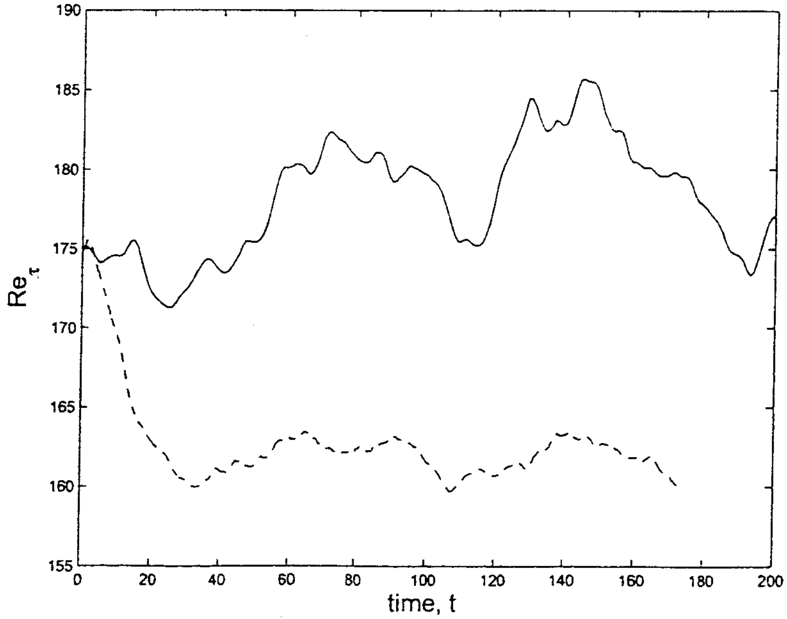

FIG. 11: Effect of aliasing error upon $\tilde{Re}_\tau$ for $128^3$ simulations. LEGEND: solid line (DNSa); dashed line (DNSb).

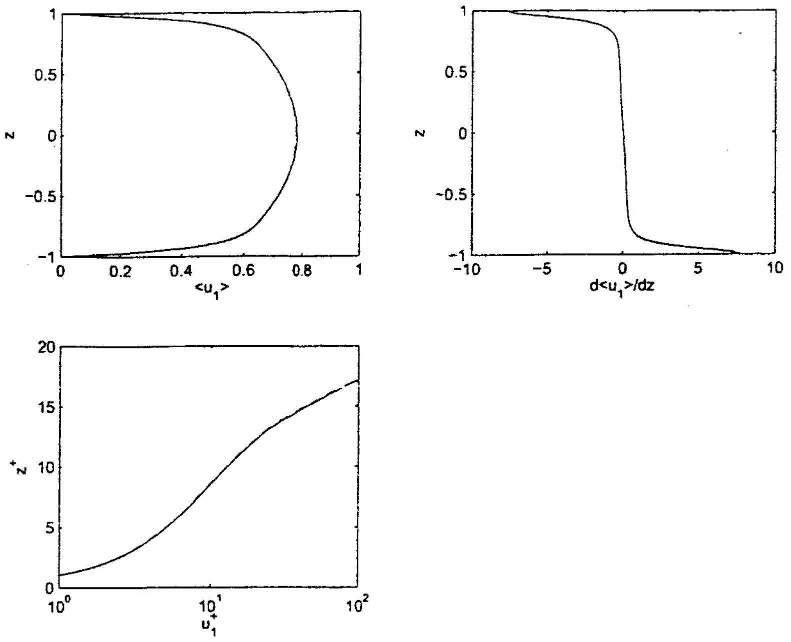

FIG. 12: Mean streamwise velocity $< u_1 >$ and its wall-normal derivative in standard and wall units for Case DNSa relative to KMM reference data. LEGEND: solid line (KMM); dashed line (DNSa). (KMM data are replicated symmetrically about centerline for clarity.)

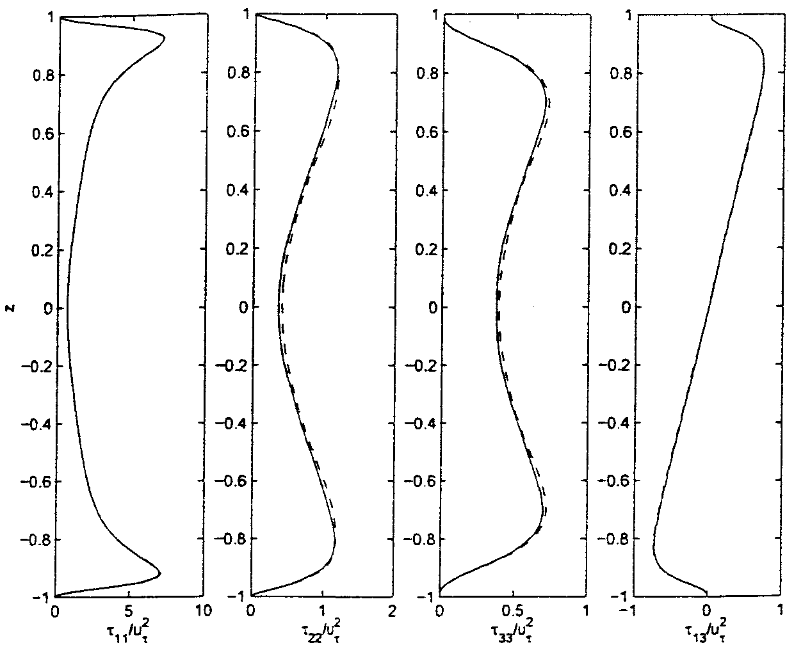

FIG. 13: Reynolds stresses of present DNS compared with reference of Moser et al. for nominal $Re_\tau = 180$. LEGEND: solid line (KMM); dashed line (DNSa). (KMM Data are replicated symmetrically about centerline for clarity.)

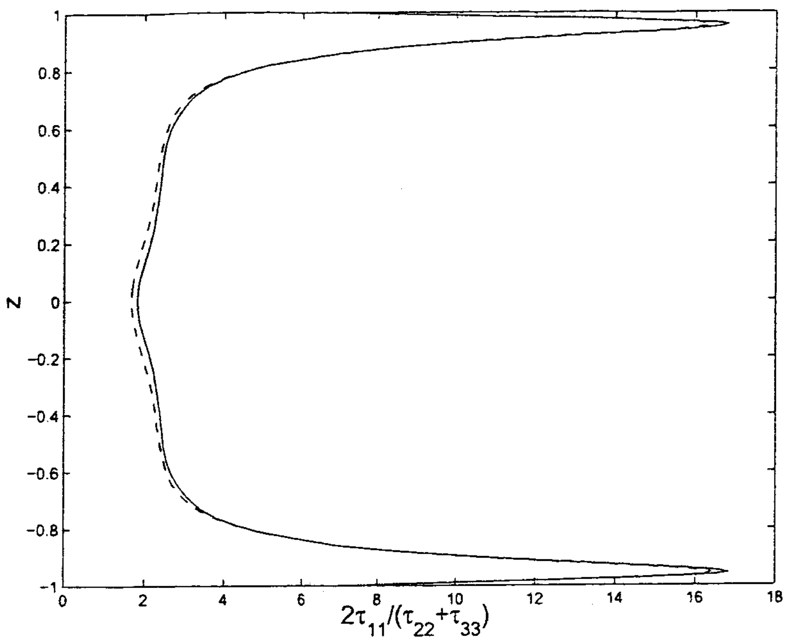

FIG. 14: Reynolds-stress ratio as a measure of anisotropy. LEGEND: solid line (KMM); dashed line (DNSa). (KMM Data are replicated symmetrically about centerline for clarity.)

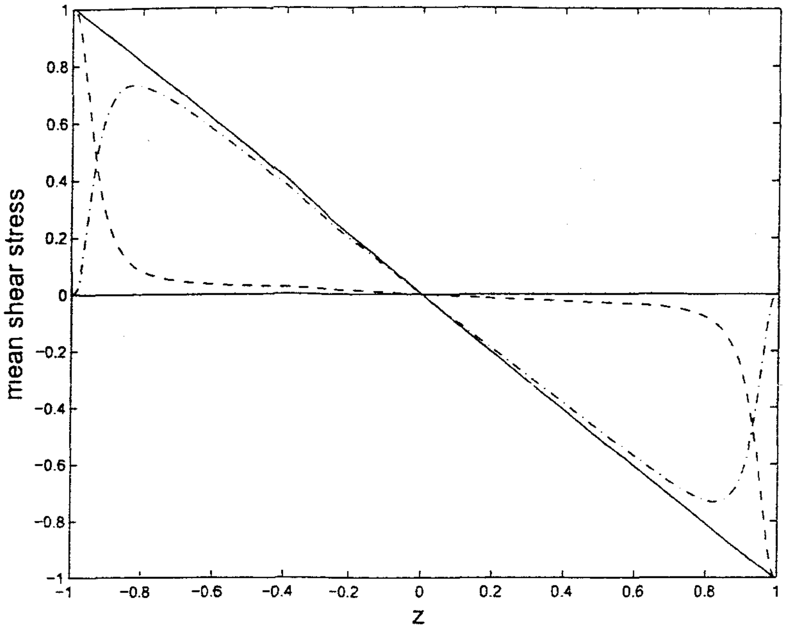

FIG. 15: Shear stress balance for Case DNSa, following Pope [22]. Figure confirms theoretical result that sum of viscous and Reynolds stresses is linear for turbulent channel flow. LEGEND: solid line (total shear stress [$= \tau/u_\tau^2$]); dashed line (viscous stress [$= du_1^+/dz$]); dashed-dotted line (Reynolds stress [$=\tau_{13}/u_\tau^2$]).

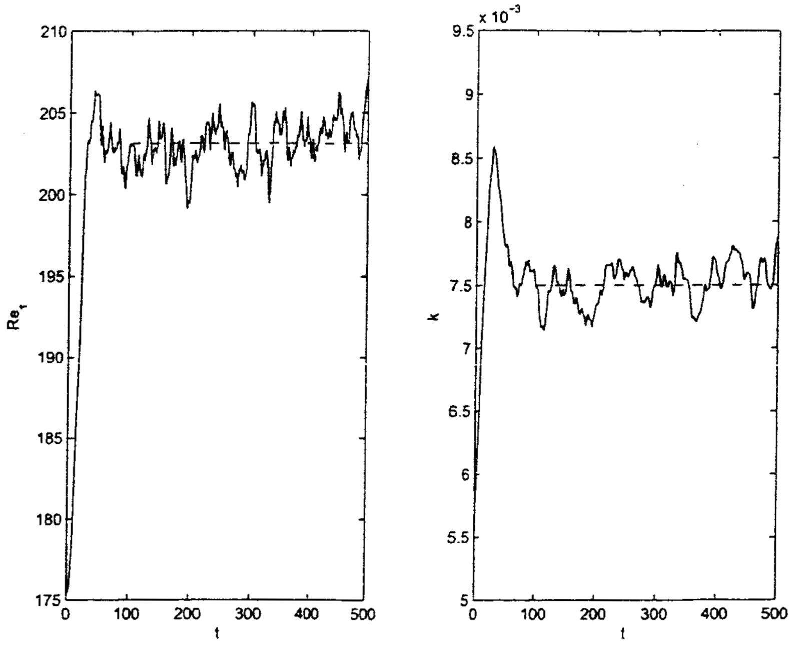

FIG. 16: Evolution of $Re_\tau$ and $k$ for Case BASEa. LEGEND: solid line (instantaneous); dashed line (mean)

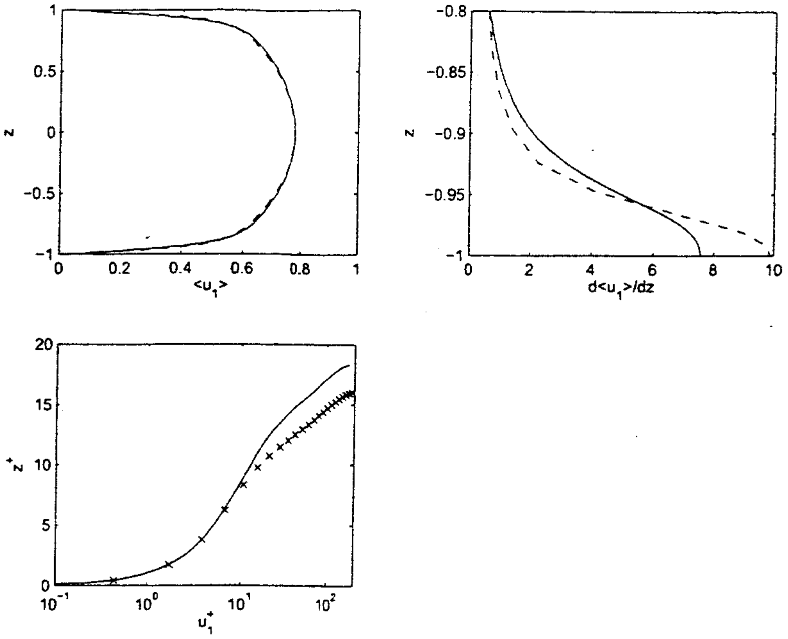

FIG. 17: Mean streamwise velocity profile $< u_1 >$ vs. $z$ and its wall-normal derivative for "no model" coarse-grid Case BASEa relative to reference data of Moser et al., presented in both standard and wall units. LEGEND: solid line (KMM); dashed line (BASEa); symbols (BASEa, wall units).

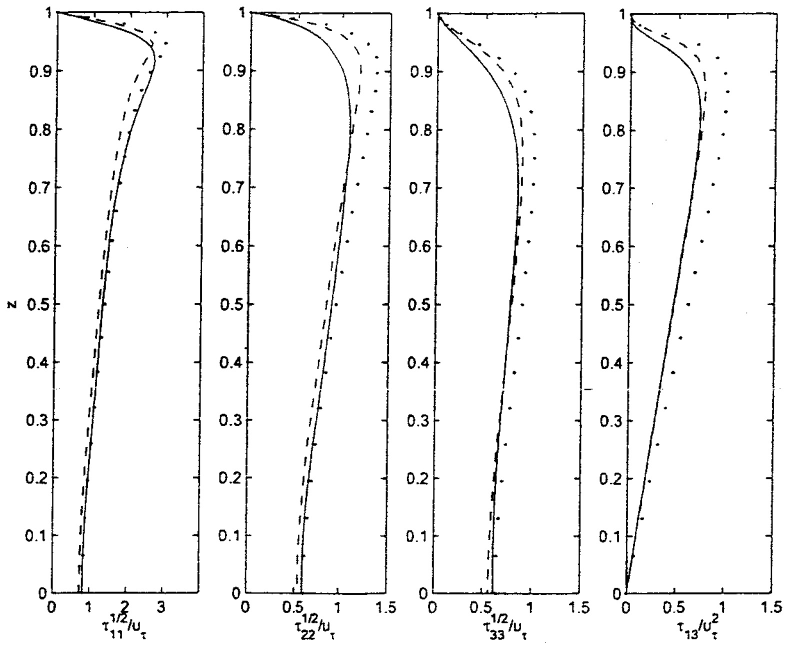

FIG. 18: Fluctuation velocities and Reynolds stresses vs. $z$ for Case BASEa relative to reference DNS data of Moser et al.: solid line (reference DNS), dotted line (BASEa scaled absolutely by $u_\tau = Re_\tau/Re_{\mathrm{lam}} = 178/4200$ of reference DNS); dashed line (BASEa scaled relatively by derived $u_\tau = Re_\tau/Re_{\mathrm{lam}} = 203/4200$).

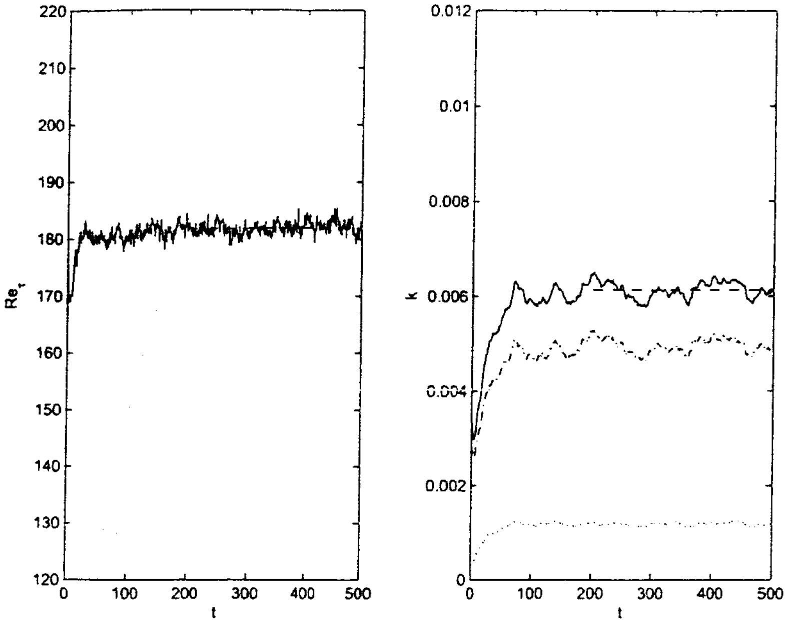

FIG. 19: Evolution of $Re_\tau$ and $k$ for Case BASEb. LEGEND: solid line (instantaneous); dashed line (mean); dashed-dotted line ($\bar{k}$); dotted line ($k_R$).

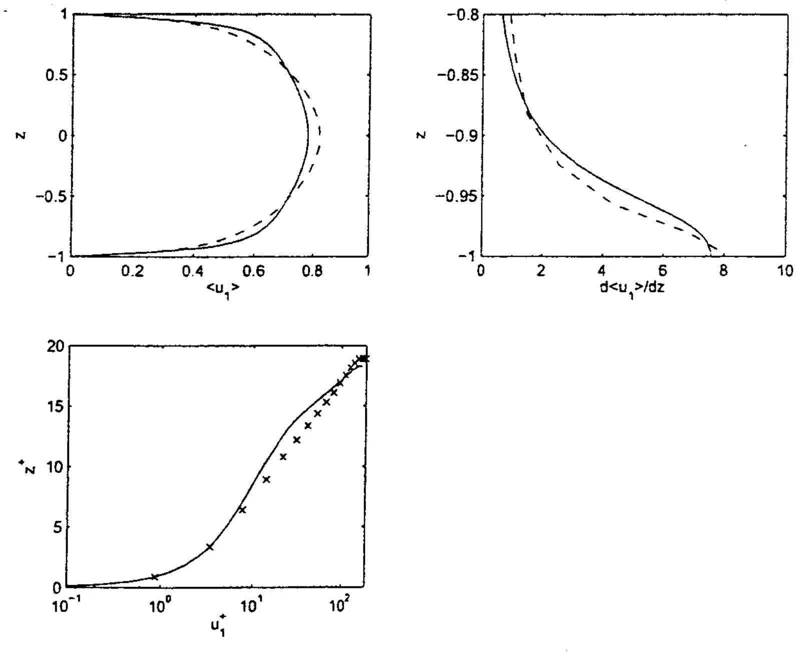

FIG. 20: Mean streamwise velocity profile $< u_1 >$ vs. $z$ and its wall-normal derivative for Case BASEb relative to reference DNS data of Moser et al. LEGEND: solid line (KMM); dashed line (BASEb); symbols (BASEb, wall units).

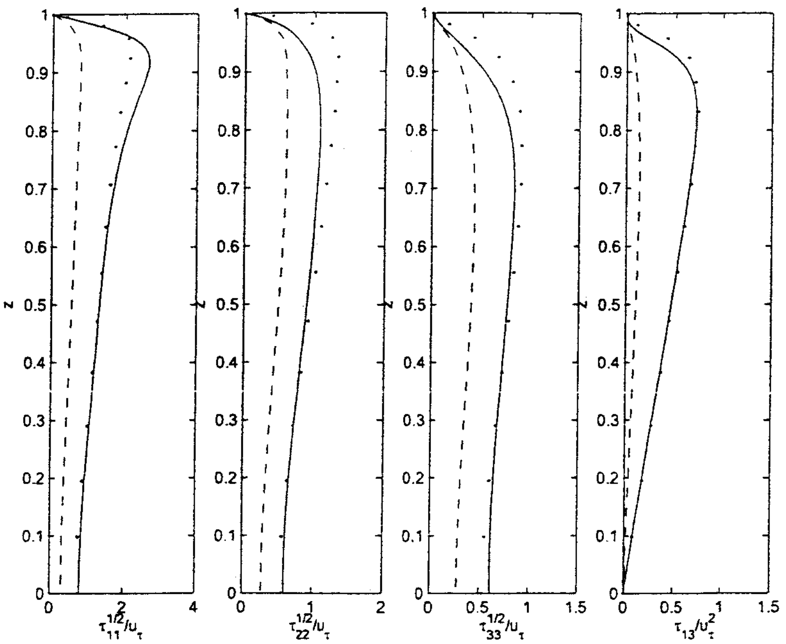

FIG. 21: Fluctuation velocities and Reynolds stresses vs. $z$ for Case BASEb relative to reference DNS data of Moser et al. LEGEND: solid line (reference DNS); dotted line ($< M_{ij} > + \bar{\tau}_{ij}$, TLES); dashed line (contribution of $< M_{ij} >$, TLES).

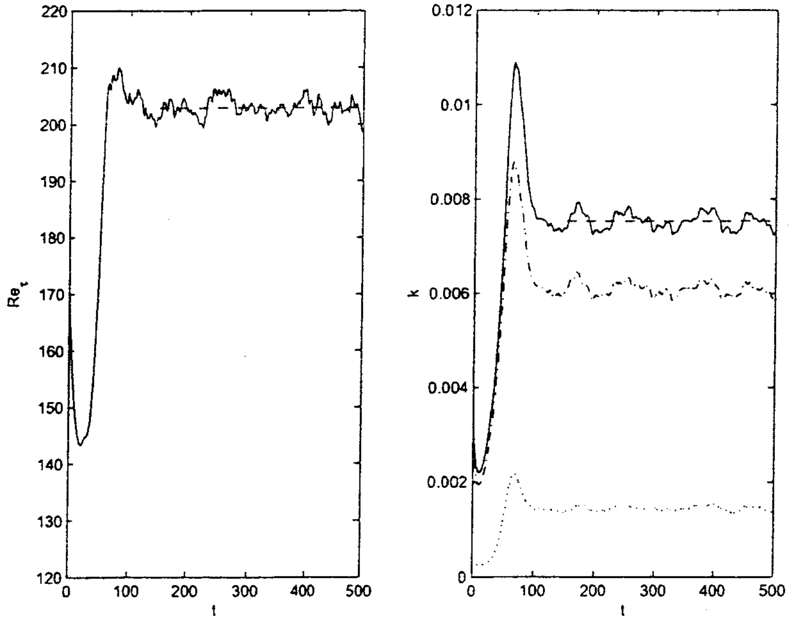

FIG. 22: Evolution of $Re_\tau$ and $k$ for Case BASEc. LEGEND: solid line (instantaneous); dashed line (mean); dashed-dotted line ($\bar{k}$); dotted line ($k_R$).

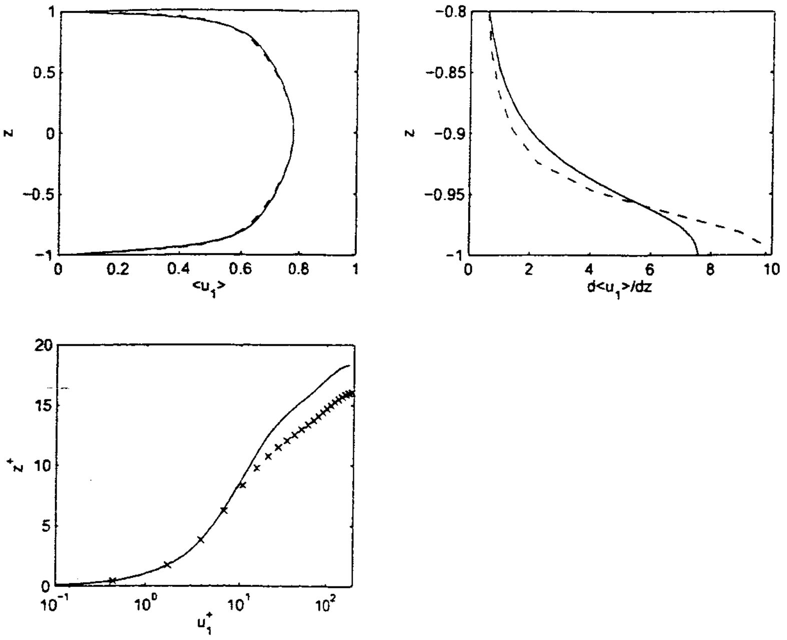

FIG. 23: Mean streamwise velocity profile $< u_1 >$ vs. $z$ and its wall-normal derivative for Case BASEc relative to reference DNS data of Moser et al. LEGEND: solid line (KMM); dashed line (BASEc); symbols (BASEc, wall units).

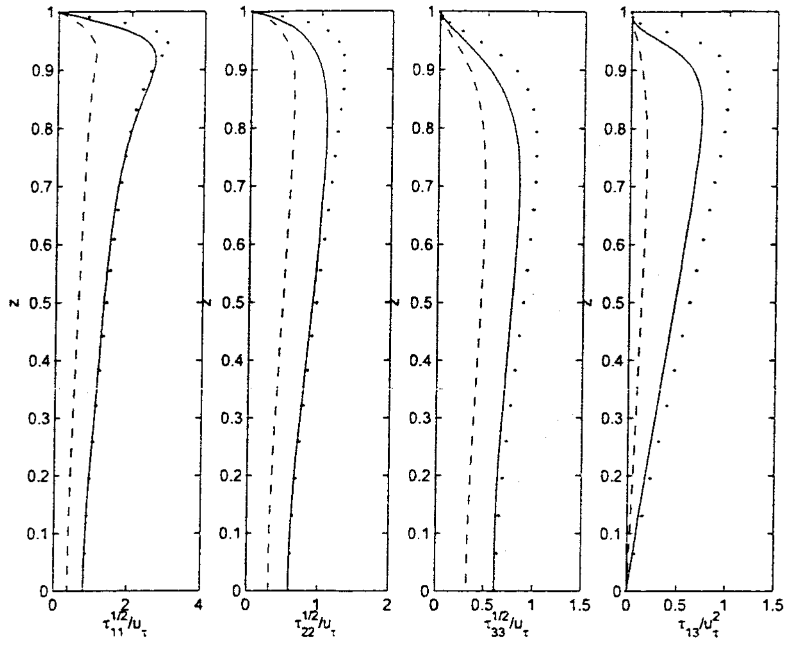

FIG. 24: Fluctuation velocities and Reynolds stresses vs. $z$ for Case BASEc relative to reference DNS data of Moser et al. LEGEND: solid line (reference DNS); dotted line ($< M_{ij} > + \bar{\tau}_{ij}$, TLES); dashed line (contribution of $< M_{ij} >$, TLES).

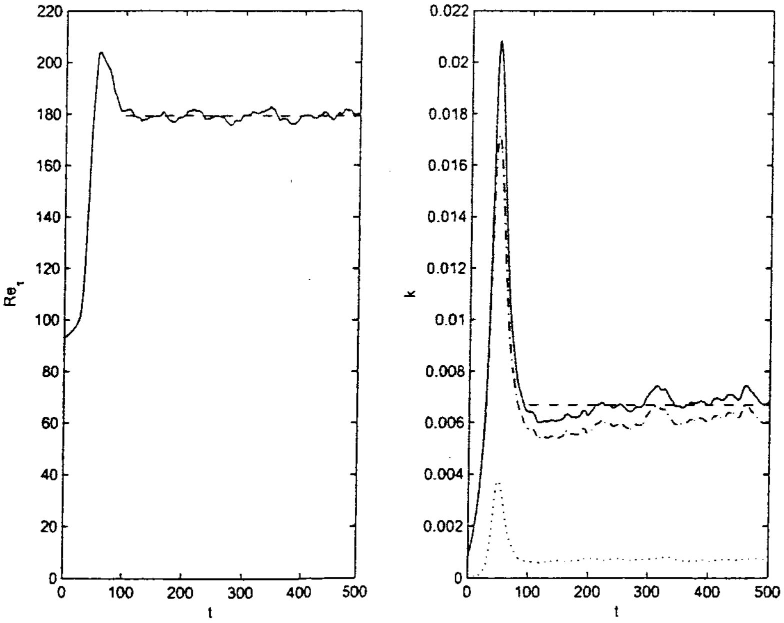

FIG. 25: Evolution of $Re_\tau$ and $k$ for Case TLES180b. LEGEND: solid line (instantaneous); dashed line (mean); dashed-dotted line ($\bar{k}$); dotted line ($k_R$).

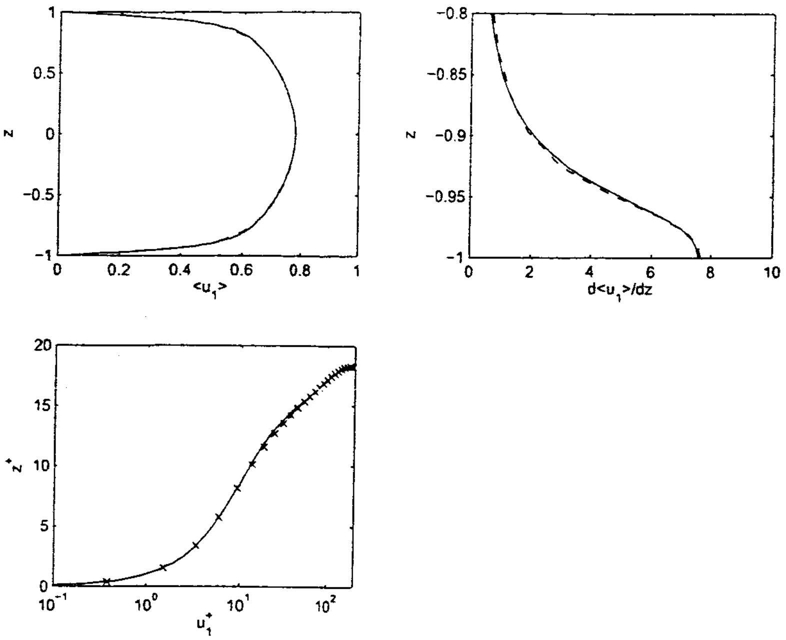

FIG. 26: Mean streamwise velocity profile $< u_1 >$ vs. $z$ and its wall-normal derivative for Case TLES180b relative to reference DNS data of Moser et al. LEGEND: solid line (KMM); dashed line (TLES180b); symbols (TLES180b, wall units).

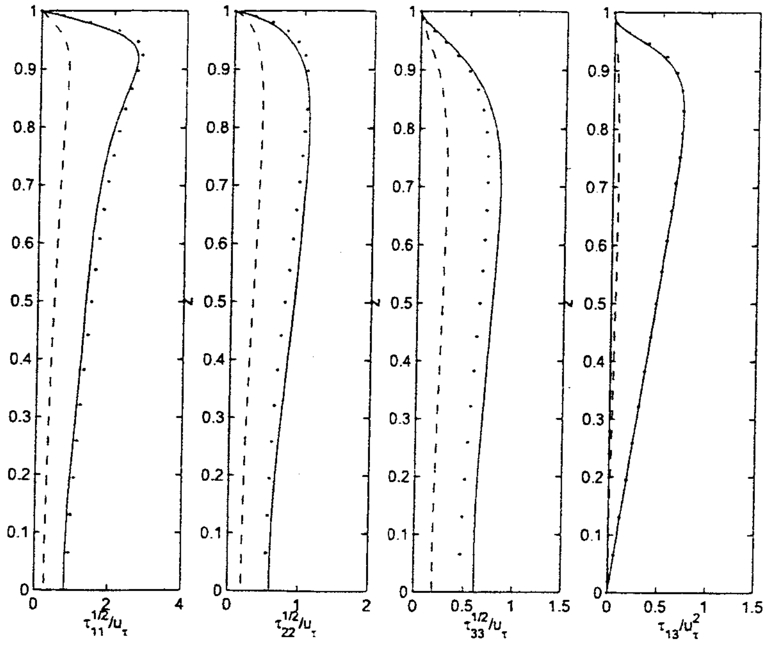

FIG. 27: Fluctuation velocities and Reynolds stresses vs. $z$ for Case TLES180b relative to reference DNS data of Moser et al. LEGEND: solid line (reference DNS); dotted line ($< M_{ij} > +\bar{\tau}_{ij}$, TLES); dashed line (contribution of $< M_{ij} >$, TLES).

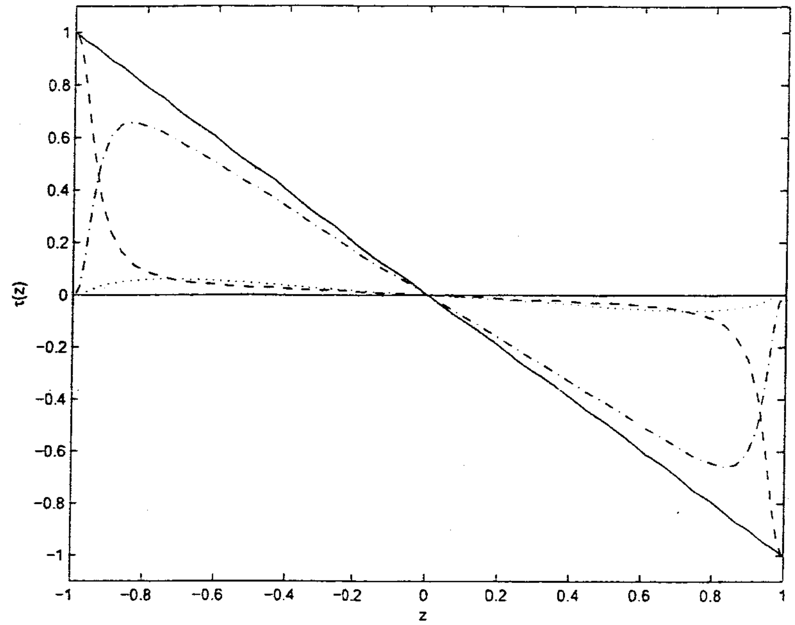

FIG. 28: Shear stress balance for Case TLES180b, following Pope [22]. Figure confirms theoretical result that sum of viscous and Reynolds stresses is linear for turbulent channel flow. LEGEND: solid line (total shear stress [= $\tau/u_\tau^2$)]); dashed line (viscous stress [= $1/Re_\tau du_1^+/dz$]); dashed-dotted line (resolved Reynolds stress [= $\bar{\tau}_{13}/u_\tau^2$]); dotted line (mean modeled residual stress [= $-<M_{13}>/u_\tau^2$]).

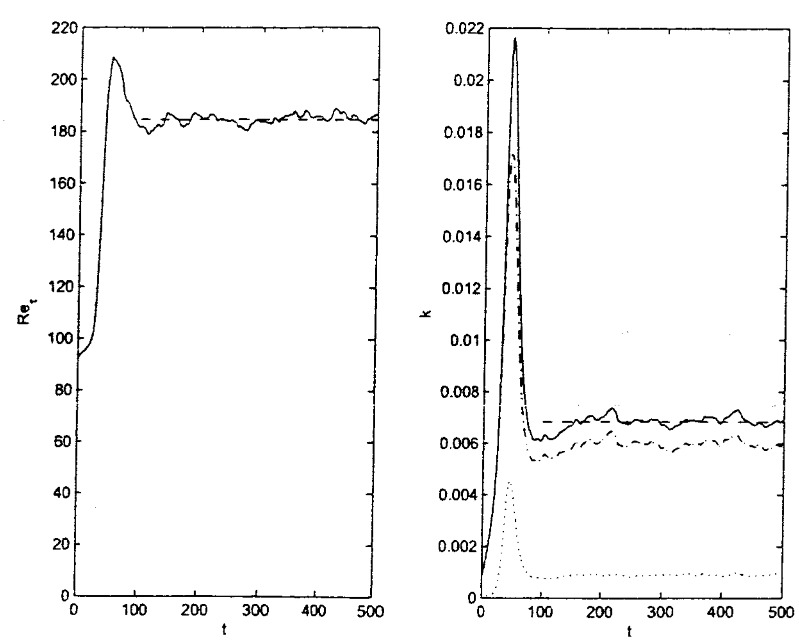

FIG. 29: Evolution of $Re_\tau$ and $k$ for Case TLES180c. LEGEND: solid line (instantaneous); dashed line (mean); dashed-dotted line ($\bar{k}$); dotted line ($k_R$).

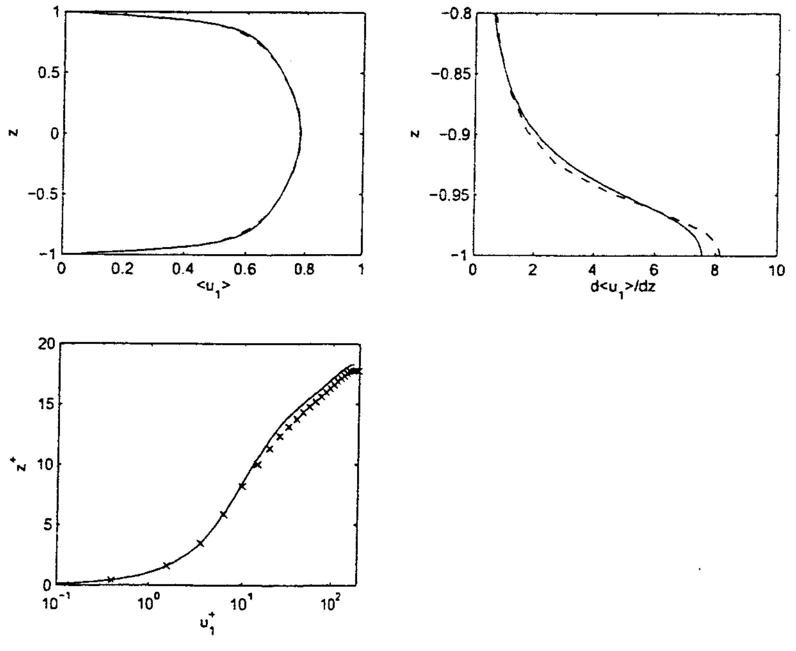

FIG. 30: Mean streamwise velocity profile $< u_1 >$ vs. $z$ and its wall-normal derivative for Case TLES180c relative to reference DNS data of Moser et al. LEGEND: solid line (KMM); dashed line (TLES180c); symbols (TLES180c, wall units).

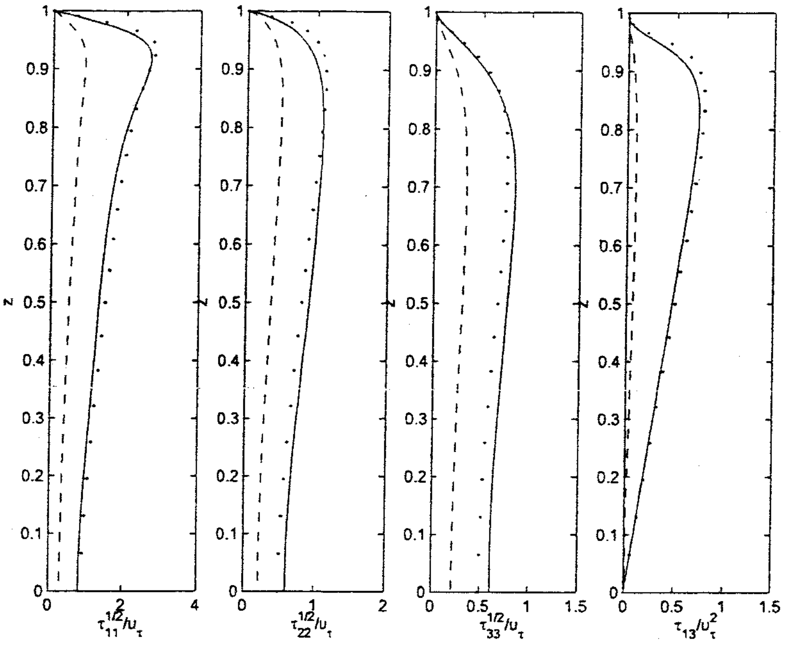

FIG. 31: Fluctuation velocities and Reynolds stresses vs. $z$ for Case TLES180c relative to reference DNS data of Moser et al. LEGEND: solid line (reference DNS); dotted line ($< M_{ij} > + \bar{\tau}_{ij}$, TLES); dashed line (contribution of $< M_{ij} >$, TLES).

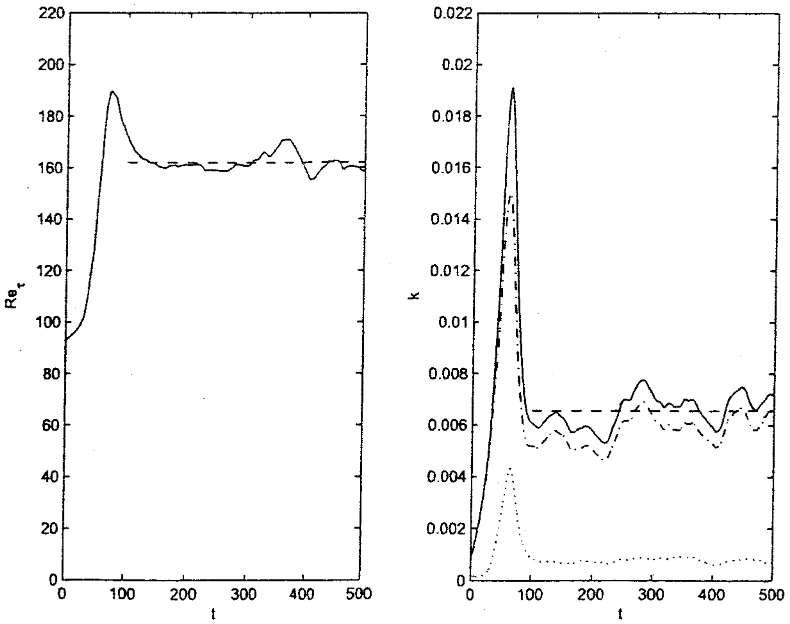

FIG. 32: Evolution of $Re_\tau$ and $k$ for Case TLESd. LEGEND: solid line (instantaneous); dashed line (mean); dashed-dotted line ($\bar{k}$); dotted line ($k_R$).

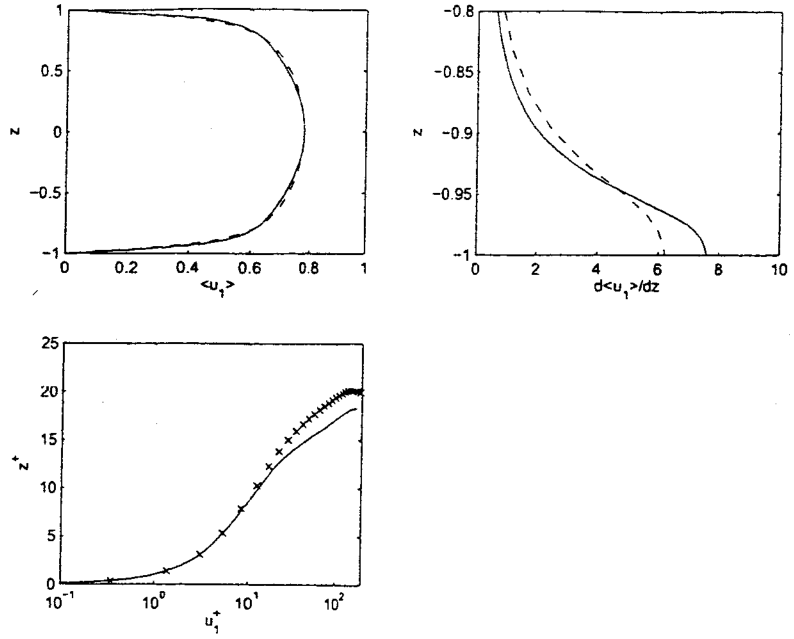

FIG. 33: Mean streamwise velocity profile $< u_1 >$ vs. $z$ and its wall-normal derivative for Case TLES180d relative to reference DNS data of Moser et al. Symbols denote values at collocation points.

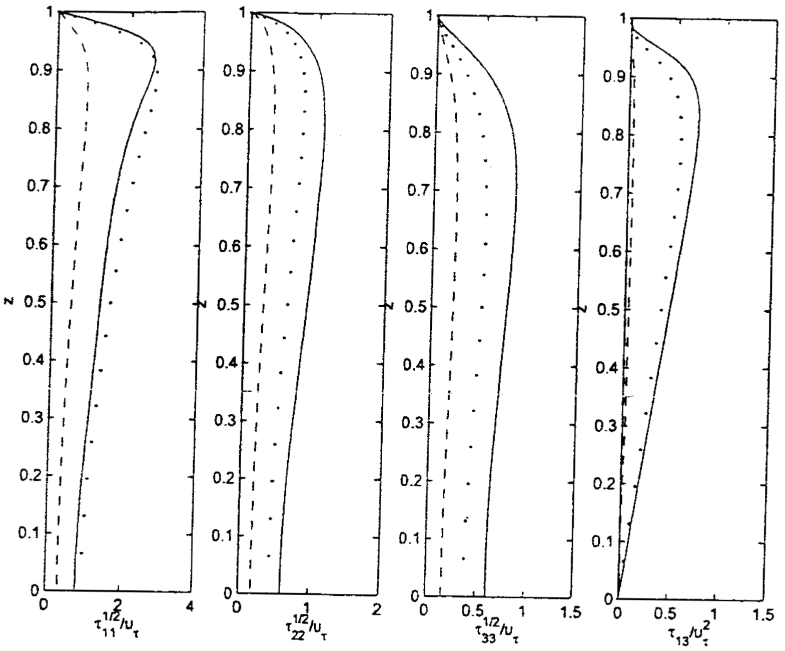

FIG. 34: Fluctuation velocities and Reynolds stresses vs. $z$ for Case TLES180d relative to reference DNS data of Moser et al. LEGEND: solid line (reference DNS); dotted line ($< M_{ij} > +\bar{\tau}_{ij}$, TLES); dashed line (contribution of $< M_{ij} >$, TLES).

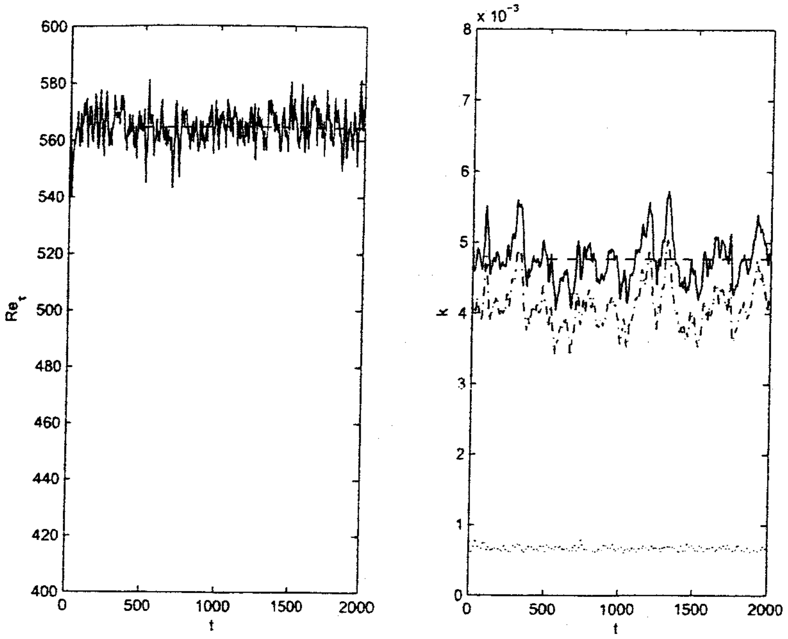

FIG. 35: Evolution of $Re_\tau$ and $k$ for Case TLES590. LEGEND: solid line (instantaneous); dashed line (mean); dashed-dotted line ($\bar{k}$); dotted line ($k_R$).

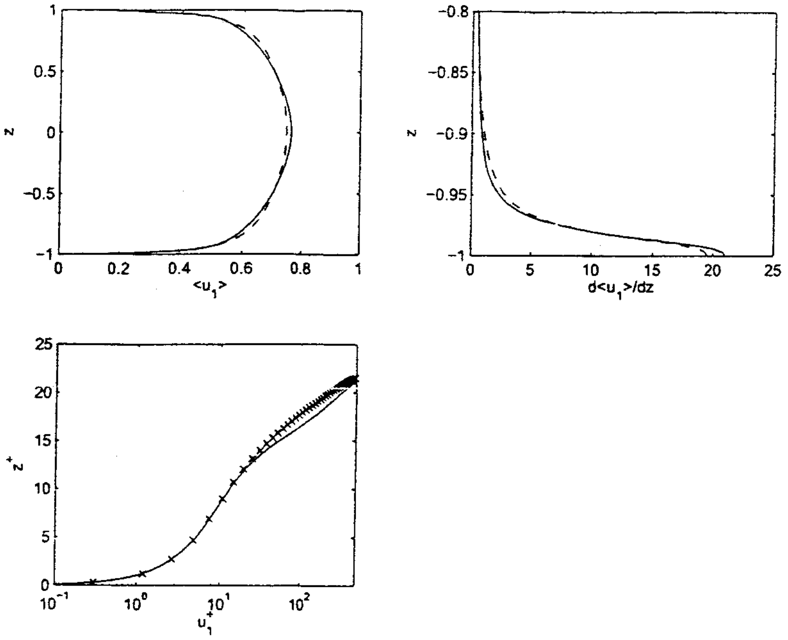

FIG. 36: Mean streamwise velocity profile $< u_1 >$ vs. $z$ and its wall-normal derivative for Case TLES590 relative to reference DNS data of Moser et al. LEGEND: solid line (KMM); dashed line (TLES590); symbols (TLES590, wall units).

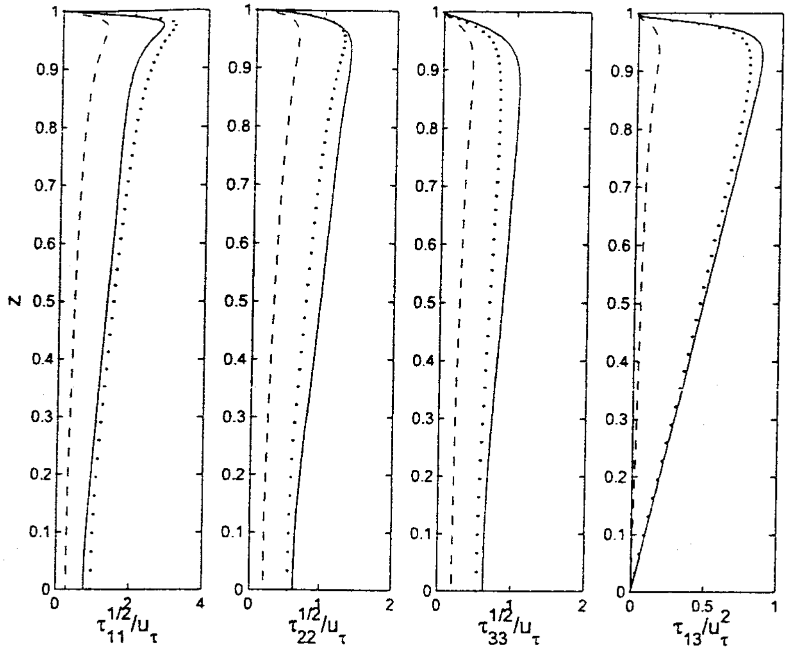

FIG. 37: Fluctuation velocities and Reynolds stresses vs. $z$ for Case TLES590 relative to reference DNS data of Moser et al. LEGEND: solid line (reference DNS); dotted line ($< M_{ij} > + \bar{\tau}_{ij}$, TLES); dashed line (contribution of $< M_{ij} >$, TLES).

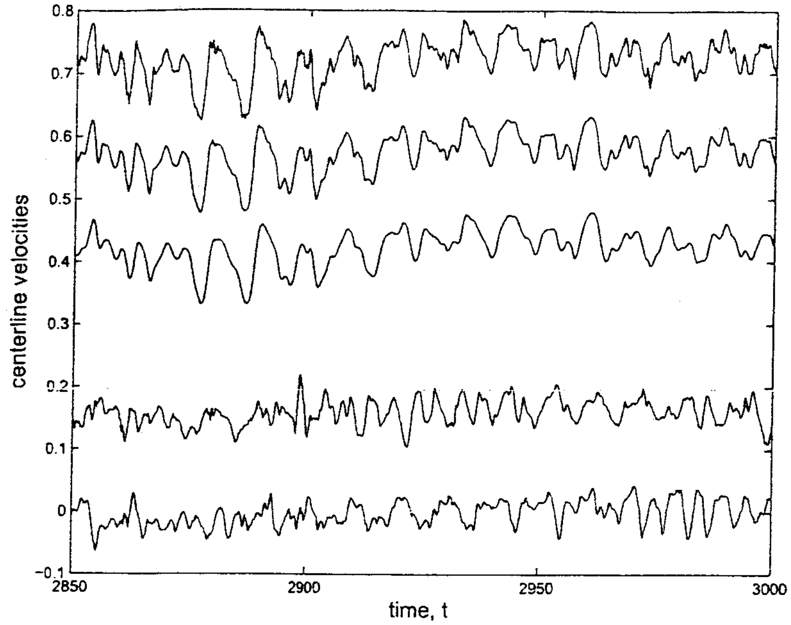

FIG. 38: Mid-plane ($z = 0$) time-trace segments of velocity components for Case TLES590. LEGEND: upper solid line ($\bar{u}_1$); fourth ($\bar{u}_1^{(2)} - 0.15$); third ($\bar{u}_1^{(3)} - 0.3$); second ($\bar{u}_2 + 0.15$); lower ($\bar{u}_3$). Selected curves shifted for clarity. Upper three traces collectively show smoothing effects of successively filtering with causal exponential filter.

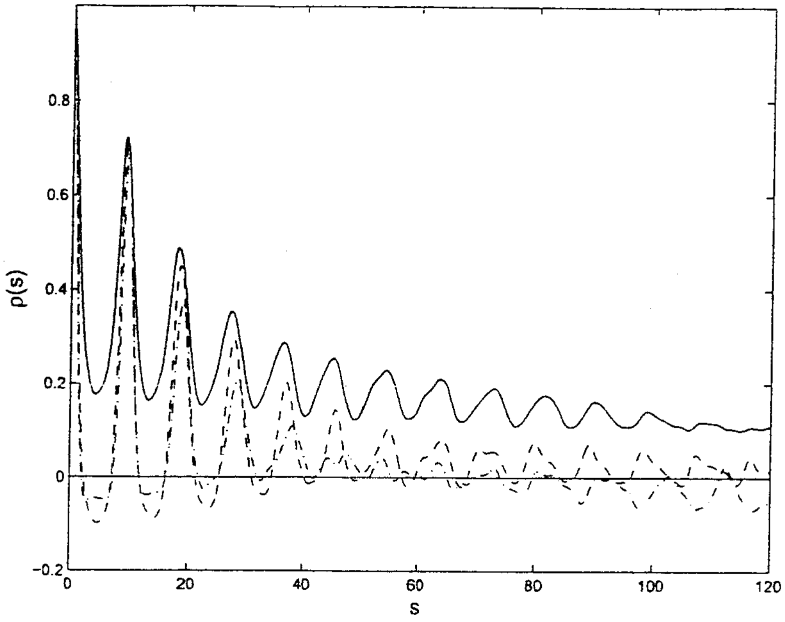

FIG. 39: Composite autocorrelation function computed from all mid-plane velocity values for Case TLES590. LEGEND: solid line ($\tilde{u}_1$); dashed line ($\tilde{u}_2$); dashed-dotted line ($\tilde{u}_3$).

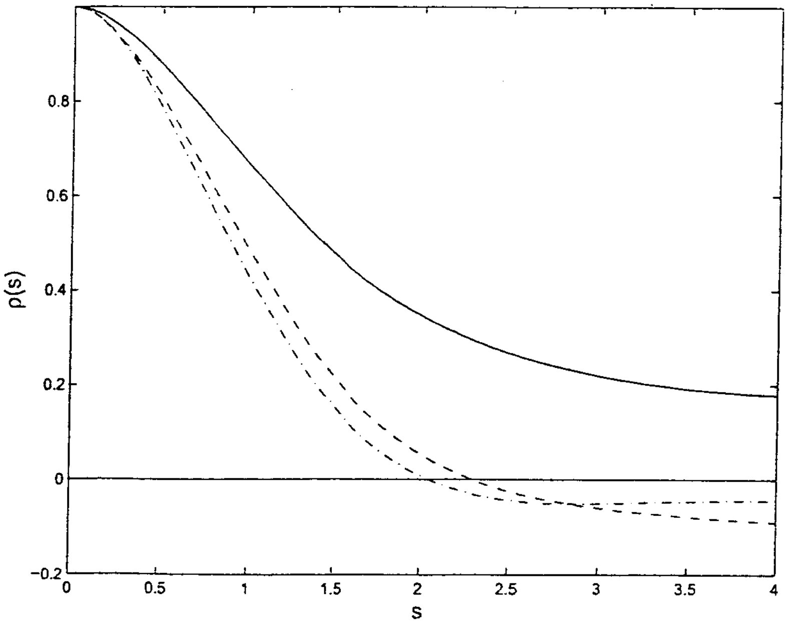

FIG. 40: Close-up of Fig. 39 near origin.

# Optimized Temporal Deconvolution*

B.C. Thomas & C.D. Pruett
*James Madison University*

An addendum to:
**Temporal Large-Eddy Simulation:**
**Final Report for NASA Grant NAG1-02033**

July 30, 2004

## 1 Introduction

Recently, Stolz and Adams (1999) revealed an approximate deconvolution model (ADM) (see also Adams and Stolz (2001)) for large-eddy simulation (LES), which has performed well in simulating flows as diverse as incompressible channel flow (Stolz et al (1999a)) and supersonic compression-ramp flow (Stolz et al (1999b); Adams (2002)), and appears to represent the state-of-the-art in residual-stress modeling. To establish a point of departure, we briefly describe the ADM.

Let $u_j$ be the fluid velocity, overbars denote linear filtering, and $\bar{u}_j^{(k)}$ denote the $k$-times successively filtered velocity. The ADM models the exact residual stress

$$R_{ij} \equiv \overline{u_i u_j} - \overline{u}_i \overline{u}_j \tag{1}$$

as $M_{ij} \approx R_{ij}$, where

$$M_{ij} = \overline{v_i v_j} - \overline{v}_i \overline{v}_j \tag{2}$$

and

$$v_j = \sum_{k=0}^{p} C_k \bar{u}_j^{(k+1)} \tag{3}$$

The quantity $v_j$, termed the deconvolved velocity, approximates $u_j$ by defiltering $\bar{u}_j$. For LES, the coefficients $C_k$ are judiciously chosen so that $v_j$ faithfully restores the low wavenumber content of $u_j$ while attenuating high-wavenumber content. Thus, the method is useful for

---

*Research supported in part by NASA Grant NAG1-02033 and by the College of Science and Mathematics, James Madison University.

LES expressly *because* it is approximate, not *despite* its being approximate. The index $p$ determines the order of the deconvolution.

Suppose $H(\xi)$ is the transfer function that defines the action of the filter in Fourier space, where $\xi = \kappa\Delta$, $\kappa$ is the wavenumber, and $\Delta$ is the filter width, which parameterizes the filter. Provided the filter is invertible ($H \neq 0$) and $|1 - H| < 1$, the transfer function has an exact power-series inverse, namely

$$H^{-1} = \frac{1}{1-(1-H)} = 1 + (1-H) + (1-H)^2 + ... + (1-H)^p + ... \tag{4}$$

Truncating the series at finite order $p$ yields the transfer function of the approximate inverse $\tilde{H}^{-1}$, namely

$$\tilde{H}^{-1} = 1 + (1-H) + (1-H)^2 + ... + (1-H)^p \tag{5}$$

The product $H * \tilde{H}^{-1}$ is the Fourier-space analog of Eq. 3. By isometry between Fourier and physical space, the coefficients $C_k$ are determined simply by the binomial theorem (Pascal's triangle); that is, for example, for $p = 3$, $[C_0, C_1, C_2, C_3] = [4, -6, 4, -1]$.

As Stolz and Adams (1999) note, the ADM (Eq. 2) can be viewed as a generalized scale-similarity model (GSSM). It is well known that similarity models are insufficiently dissipative without secondary regularization (high-order artificial viscosity) and tend to produce numerical instabilities. Stabilization is accomplished in the original ADM by the addition of a dissipative term to the right-hand side of the momentum equations, namely

$$-\chi(u_j - v_j) \tag{6}$$

where $\chi$ is an arbitrary damping parameter, to be determined. Thus, in the ADM, deconvolution serves two distinct purposes:

1. Modeling of the residual stress
2. Generation of high-order artificial viscosity

In Fourier space, the operators associated with the two purposes above are, respectively

1. $H * \tilde{H}^{-1}$
2. $1 - H * \tilde{H}^{-1}$

If the filter is based upon a symmetric stencil, the transfer function $H$ is purely real, as are $H * \tilde{H}^{-1}$ and $1 - H * \tilde{H}^{-1}$.

Let $H_p^{-1}$ denote the approximate inverse of order $p$. Figure 1 presents the transfer function of a centered, second-order, parameterized Padé filter, with the nominal cutoff set at $\xi_c = \pi/2$. Also shown are the exact inverse, the approximate inverse for $p = 3$, and the two operators of interest: $H * \tilde{H}^{-1}$ and $1 - H * \tilde{H}^{-1}$. Strictly speaking, $H$ is not invertible; consequently, its exact inverse is unbounded. However, its approximate inverse is well-defined for all finite orders $p$.

In closing this section, the point to be made is that the "Pascal" coefficients serve well in both capacities of the deconvolution: modeling and dissipation. The operator $H * \tilde{H}^{-1}$

manifests desirable low-pass properties: it is unity at $\xi = 0$, is flat in the vicinity of the origin (which indicates that low wavenumber content is faithfully recovered by defiltering), and drops off rapidly to zero at high wavenumbers. Because symmetric spatial filtering induces no phase error, $u_j$ and $v_j$ are aligned in phase, and the operator $1 - H * \tilde{H}^{-1}$ is purely real. The product of $\chi(1 - H * \tilde{H}^{-1})$ quantifies the exponential decay rate as a function of wavenumber. If $1 - H * \tilde{H}^{-1}$ is of one sign (as it is for the Pascal coefficients), and $\chi > 0$, then secondary regularization is purely dissipative, with the dissipation concentrated at high wavenumbers (Fig. 1).

In the next sections, we describe modifications necessary to adapt approximate deconvolution from spatial to time-domain filtering. The resulting temporal variant of the ADM will be referred to as the TADM; similarly, LES with with the TADM will be termed TLES (temporal LES).

## 2 Causal Time-Domain Filtering

Consider an exponential causal filter expressed in differential form, namely

$$\frac{d\bar{u}_j}{dt} = \frac{u_j - \bar{u}_j}{\Delta} \tag{7}$$

and parameterized by the temporal filter width $\Delta$. The transfer function of the continuous filter above is

$$H(\omega; \Delta) = \frac{1}{1 + i\omega\Delta} \tag{8}$$

where $\omega$ is the dimensional circular frequency and $i = \sqrt{-1}$.

When the filter is implemented by the discrete solution of Eq. 7 with time increments $\Delta t$, it is natural to re-parameterize in terms of the filter-width ratio $r = \Delta/\Delta t$, in which case the transfer function becomes

$$H(\Omega; r) = \frac{1}{1 + ir\Omega} \tag{9}$$

where $\Omega = \omega\Delta t$. If the ODE is solved accurately, say, by a high-order numerical method such as fourth-order Runge-Kutta, then the transfer function of the fully discretized problem is virtually identical to Eq. 9, so that the continuous transfer function may be used for purposes of analysis.

Whereas spatial filters with symmetric stencils are characterized by purely real transfer functions, causal filters have complex transfer functions, because they are by definition biased in time, as, for example, in Eq. 9. As a consequence, causal filtering produces both amplitude attenuation (desired) and phase error (undesired). The phase shift $\phi$ of the exponential filter above is given by

$$\phi(\Omega; r) = \tan^{-1}\left(\frac{-H_i}{H_r}\right) = -\tan^{-1}(r\Omega) \tag{10}$$

Because of the phase error associated with causal filtering and subtle differences between the transfer functions of causal and spatial filters, both components of the ADM (residual-stress modeling and secondary regularization) require modification when adapted for time-domain filtering. This presents two possible approaches to addressing the problem: either a single deconvolution for both purposes, or independent deconvolutions, each designed for a specific purpose. Here we follow the latter path. Dual deconvolutions require some additional storage but no appreciable additional computational effort. The next two sections address deconvolution optimizations for residual-stress modeling and secondary regularization, respectively.

## 3 Residual-Stress Model

Formally, the residual-stress model of the TADM is identical to Eq 2. Phase error is not problematic for the residual-stress model, because both terms of Eq. 2 have the same phase relationships. On the other hand, because $H$ (see Eq. 9) is complex for causal filters, other problems arise for which adjustments must be made.

Recall that in Fourier space, the approximate inverse of $H$ is given by

$$\tilde{H}^{-1} \approx \sum_{k=0}^{p} C_k H^k \tag{11}$$

Insight into the efficacy of the deconvolution can be gained through analysis of the operator $H * \tilde{H}^{-1}$, which is complex. Ideally, for applications to LES, the modulus $|H * \tilde{H}^{-1}|$ is shaped like a spectral (sharp cutoff) low-pass filter. The closer the operator approximates this ideal, the better the residual-stress model is likely to be, as implied by Fig. 2, which presents $|H|$ and $|H * \tilde{H}^{-1}|$ relative to the spectral ideal for a deconvolution of order $p = 3$. The ideal exactly restores low wavenumber content (resolved scales) while attenuating energy at high wavenumbers (unresolved scales) to zero.

The Pascal coefficients of the ADM are unsuitable for the TADM as shown in Fig. 3. Not only is energy at moderate wavenumber not attenuated, it is amplified. Thus, an optimized TADM requires that the coefficients $C_k$ be expressly engineered to give $H * \tilde{H}^{-1}$ "near-ideal" properties.

To illustrate the design process, consider a third-order deconvolution (i.e., $p = 3$). The parameter space consists initially of the four free parameters $[C_0, C_1, C_2, C_3]$. The requirement that the coefficients sum to unity reduces the parameter space by one. That is,

$$C_3 = 1.0 - (C_0 + C_1 + C_2) \tag{12}$$

The remaining coefficients are found by forcing to zero successive derivatives of the modulus of $H * \tilde{H}^{-1}$, which flattens its graph in the vicinity of the origin.

There is, however, a further consideration that involves the the zeroth coefficient, $C_0$. Unlike spatial filters, such as the Padé filter shown previously, causal filters do not in general vanish identically at the Nyquist frequency ($\Omega = \pi$); rather, they tend toward zero asmyptotically as $\Omega \rightarrow \infty$, as, for example, in Eq. 9. Because all terms of $\tilde{H}^{-1}$ except the zeroth-order term contain $H$ (see Eq. 11), $\tilde{H}^{-1} \rightarrow C_0$ as $\Omega \rightarrow \infty$, and if $C_0 \neq 0$, $H * \tilde{H}^{-1}$ tends toward zero as $1/\Omega$. For example, with $C_0 = 1$, $H * \tilde{H}^{-1} \rightarrow H$ as $\Omega \rightarrow \infty$, as seen in Figure 2. However, by setting $C_0 = 0$, attenuation at high frequencies increases to $1/\Omega^2$, which is highly desirable (Fig. 4). From a physical point of view, setting $C_0 = 0$ implies that the deconvolved velocity is re-constructed only from fields that have been low-pass filtered at least twice. This ensures that the process of deconvolution is stable at high frequency.

At this point, only $C_1$ and $C_2$ remain free parameters. These are determined by setting the second and fourth derivatives of the modulus of $H * \tilde{H}^{-1}$ to zero (as the odd derivatives are automatically zero). Algebraic constraint equations can be readily derived by use of computer algebra software. In general, the resulting equations are nonlinear and admit multiple solutions. Complex solutions, which are discarded because they cannot be readily implemented in physical space, occur in conjugate-symmetric pairs. The remaining real solutions yield approximate inverses $\tilde{H}^{-1}$ that share the same moduli but differ in phase. In particular, for $p = 3$, the method described herein yields two real and two complex solutions, from which the following set of real coefficients is selected as optimal: $[0.0, \sqrt{6}, \sqrt{4 + 2\sqrt{6}} - 2\sqrt{6}, 1 - \sqrt{4 + 2\sqrt{6}} + 2\sqrt{6}]$. Figure 4 presents the moduli of $H$, $\tilde{H}^{-1}$, and $H * \tilde{H}^{-1}$ for this coefficient set. The zero-valued derivatives of $|H * \tilde{H}^{-1}|$ force its graph to be as flat as possible at low frequencies, while the value of zero for $C_0$ causes the sharp drop-off at higher frequencies. The resulting effect is an amplitude restoration near zero, and a greater attenuation at high frequencies (Fig. 4).

Obviously the method can be extended to higher order deconvolution.

Experience to date suggests that the temporal residual-stress model is more than adequate. Deconvolution orders of 2, 3, 4, and 5 have been examined, as have a variety of deconvolution coefficients and filter widths. In all cases, the instantaneous and mean residual stresses are well defined, with mean components that have qualitatively correct profiles. In sum, temporal deconvolution appears to admit a family of robust residual-stress models.

## 4 Secondary Regularization

The purpose of secondary regularization is to impose high-order artificial viscosity at high frequencies while leaving low frequencies relatively undisturbed.

Consider the complex exponential function $u(t) = e^{i\omega t}$, which satisfies the complex differential equation of a harmonic oscillator, namely

$$\frac{du}{dt} = i\omega u \tag{13}$$

Secondary regularization functions as a dissipative term for a harmonic oscillator. Accordingly, consider the model problem

$$\frac{du}{dt} = i\omega u - \chi(u - H * \tilde{H}^{-1} u) = [i\omega + \chi(H * \tilde{H}^{-1} - 1)]u$$

The additional term, the Fourier-space analog of Eq. 6, imposes exponential damping provided

$$Re[i\omega + \chi(H * \tilde{H}^{-1} - 1)] < 0.0$$

which is satisfied iff

$$Re[\chi(H * \tilde{H}^{-1} - 1)] < 0.0$$

or

$$Re[H * \tilde{H}^{-1}] < 1.0 \tag{14}$$

The exponential envelope (e.g. $e^{\lambda t}$) of the damped harmonic oscillation is governed by the decay rate $\lambda(\Omega) = \chi * [Re(H * \tilde{H}^{-1}) - 1]$, which in turn is scaled by the damping parameter $\chi$.

Constraint Eq. 4 is violated whenever the Pascal coefficients are used in secondary regularization in the TADM. As shown in Fig. 5, the decay rate is positive for some frequencies, which leads to unstable exponential growth in time.

For a given order $p$, optimal coefficients can be found by setting derivatives of the real part of $H * \tilde{H}^{-1}$ to zero, which, once again, is readily accomplished using computer algebra software. For example, for $p = 3$, there are four coefficients, three of which are free parameters. Optimal coefficients are found by forcing the second, fourth, and sixth derivatives of Re$[H * \tilde{H}^{-1}]$ to zero. (Odd-order derivatives are automatically zero.) Specifically, the optimal coefficients for third-order temporal secondary regularization are $[C_0, C_1, C_2, C_3] = [\frac{35}{16}, \frac{-29}{16}, \frac{3}{4}, \frac{-1}{8}]$. The decay rate for this coefficient set is shown in Fig. 6 (for a $\chi$ of unity). Similarly, an optimal set of coefficients for second-order ($p = 2$) secondary regularization is $[C_0, C_1, C_2] = [\frac{15}{8}, \frac{-9}{8}, \frac{1}{4}]$. Figure 6 also presents the decay rate for optimized $p = 2$ secondary deconvolution.

# 5 Results

Figures 7, 8, and 9 compare results of TLES at nominal $Re_\tau = 590$ to reference channel-flow data from DNS by Moser et al (1988). Parameter values for the TLES and reference simulations are presented in Table 1. The TLES is conducted with a TADM of order $p = 3$ with distinct coefficient optimizations for residual-stress modeling (coefficients $[0.0, 2.4495, -1.9159, 0.4664]$) and secondary regularization (coefficients $[\frac{35}{16}, \frac{-29}{16}, \frac{3}{4}, \frac{-1}{8}]$), as discussed in the previous two sections. The flow is initialized to a laminar state, randomly perturbed. Mean quantities are computed by averaging over $500 \leq t \leq 1500$. Spatial resolution for the TLES is commensurate with that of the spatial LES of channel flow with the ADM by Stolz et al (1999a), whose results are also presented in Table 1.

| Case | $N_x \times N_y \times N_z$ | $\Delta t$ | $Re_{\text{bulk}}$ | $Re_\tau$ | model | $(r, \chi)$ |
|---|---|---|---|---|---|---|
| KMM | 384 × 384 × 257 | — | 10935 | 587 | none | NA |
| SAK | 48 × 64 × 65 | — | 10935 | 574 | ADM | NA |
| TLES | 48 × 64 × 65 | 0.04 | 10935 | 595 | TADM | (8,1.0) |

Table 1: Parameter values of channel-flow TLES at nominal $Re_\tau = 590$ and reference simulations of Moser et al (1988) (KMM) and Stolz et al (1999a) (SAK).

The present results of TLES with the TADM are highly encouraging. With optimized secondary regularization, the TADM is sufficiently robust to survive the enormous spike in turbulent kinetic energy $k$ during transition (Fig. 7). The TADM adjusts accordingly during transition as indicated by the spike in $k_R$ (the trace of the modeled residual-stress tensor $M_{ij}$) during the time interval $50 \leq t \leq 150$. The computed value of $Re_\tau = 595$ deviates only 1.3 percent from the reference value of 587, an overshoot commensurate with the undershoot of the results of Stolz et al (1999a) using the ADM. Meanflow profiles are quite good near the wall but deviate somewhat from the DNS results near center channel (Fig. 8). Reynolds-stress profiles agree well qualitatively and quantitatively with DNS reference profiles (Fig. 9), with significant contribution to the Reynolds stress from the mean residual stress.

Table 2 summarizes results from several simulations of the present method (TLES) at nominal $Re_\tau = 180$, for which, for brevity, no figures are presented. Results from a reference LES of Stolz et al (1999a) using the spatial ADM are also provided. All simulations were conducted at a spatial grid resolution of $32 \times 32 \times 33$, whereas the reference DNS of Moser et al (1988), for which $Re_\tau = 178.1$, was conducted at resolution $128 \times 128 \times 129$.

The results of TLES (with optimized coefficients) at nominal $Re_\tau = 180$ are somewhat disappointing relative to the results at nominal $Re_\tau = 590$. All trial cases represent improvement over the "no-model" case (TLES180a), in which both the residual-stress model and secondary regularization are turned off. However, computed $Re_\tau$ is nearly 10 percent in error for Case TLES180b, which has the same deconvolution coefficients as for the $Re_\tau = 590$ simulation presented previously. It should be noted that, although $Re_\tau = 590$ represents a more computationally intensive calculation than $Re_\tau = 180$, $Re_\tau = 180$ may represent the more severe test of the TADM, because barely turbulent flow is in general more anisotropic than highly turbulent flow. Comparison of Cases TLES180b-c reveals the solution to be relatively insensitive to the damping coefficient $\chi$, although slightly improved by higher dissipation. Because the damping coefficient is arbitrary, this is a positive result; it would be highly undesirable for the solution to depend sensitively on an arbitrary value. (Note that the ADM also involves an arbitrary coefficient for secondary regularization, to which the solution is also relatively insensitive.)

Case TLES180d results from mixed deconvolution coefficients, where optimized third-order ($p = 3$) coefficients are exploited for the residual-stress model, but second-order ($p = 2$) optimization is used for secondary regularization. Note that both deconvolutions have the same number of free parameters (namely two), which in each case is used to force appropriate second and fourth derivatives to zero at the origin. That Case TLES180d represents further improvement suggests that higher order deconvolution is not necessarily better with regard to artificial dissipation. Here we interject some speculation. So called mixed models of residual stress blend a scale-similarity model with a Smagorinsky-like dissipative term (secondary regularization) as an attempt to fix the inadequate dissipation of a stand-alone scale-similarity model. The result is typically overly dissipative, in our view, because the dissipation comes in at second order. Our current thinking is that the dissipative term needs to be of higher order than the second derivative (at which the physical viscosity is active), but not necessarily of very high order.

In conclusion, the present addendum outlines the constraints that should be imposed

| Case | $\vec{C_2}$ | $\chi$ | $Re_\tau$ | model |
|---|---|---|---|---|
| TLES180a | N/A | N/A | 203.0 | none |
| TLES180b | [2.1875, -1.8125, 0.7500, -0.1250] | 1.0 | 195.4 | TADM |
| TLES180c | [2.1875, -1.8125, 0.7500, -0.1250] | 2.0 | 193.5 | TADM |
| TLES180d | [1.8750, -1.1250, 0.2500, 0.0] | 1.0 | 189.8 | TADM |
| SAK180a | N/A | N/A | 173. | ADM |

Table 2: Results for various trials at nominal $Re_\tau = 180$, with order $p = 3$, filter-width ratio $r = 8$, $Re_{\text{bulk}} = 2800$, vector of coefficients in residual-stress model $\vec{C_1} = [0.0, 2.4495, -1.9159, 0.4664]$, and vector of coefficients in secondary regularization $\vec{C_2}$ as indicated.

to optimize temporal deconvolution in the TADM for the dual purposes of residual-stress modeling and secondary regularization. We have focused on third-order ($p = 3$) deconvolutions, but the optimization approach is applicable to any order $p$. Furthermore, we have experimented very little with the filter-width ratio $r$, which remains an essential parameter of the TADM. Consequently, present coefficients should not be considered ideal in any sense. In sum, TLES with the TADM appears to be a promising alternative to LES that affords considerable opportunity for refinement.

## Acknowledgments

The authors are thankful to L. Kleiser and P. Schlatter of ETH Zurich for permission to use the channel-flow simulation code TRANSIT and for help in using TRANSIT, respectively. This work benefited greatly from discussions with and the insights of C. Grosch, Old Dominion University.

## References

N. A. Adams, "The use of LES subgrid-scale models for shock capturing," International Journal for Numerical Methods Fluids 39, 783 (2002).

N. A. Adams and S. Stolz, "Deconvolution methods for subgrid-scale approximation in LES," in *Modern Simulation Strategies for Turbulent Flows*, ed. B. J. Geurts, R. T. Edwards Publishing, 21 (2001).

R. D. Moser, J. Kim, N. N. Mansour, "Direct numerical simulation of turbulent channel flow up to $Re_\tau = 590$," Phys. Fluids 11, 943 (1999).

S. Stolz and N. A. Adams, "An approximate deconvolution procedure for large-eddy simulation," Phys. Fluids A 11, 1699 (1999).

S. Stolz, N. A. Adams, and L. Kleiser, "An approximate deconvolution model for large-eddy simulations with application to incompressible wall-bounded flows," Phys. Fluids **13**, 997 (2001).

S. Stolz, N. A. Adams, and L. Kleiser, "The approximate deconvolution model for large-eddy simulations of compressible flows and its application to shock-turbulent-boundary-layer interaction," Phys. Fluids **13**, 2985 (2001).

# 6 Figures

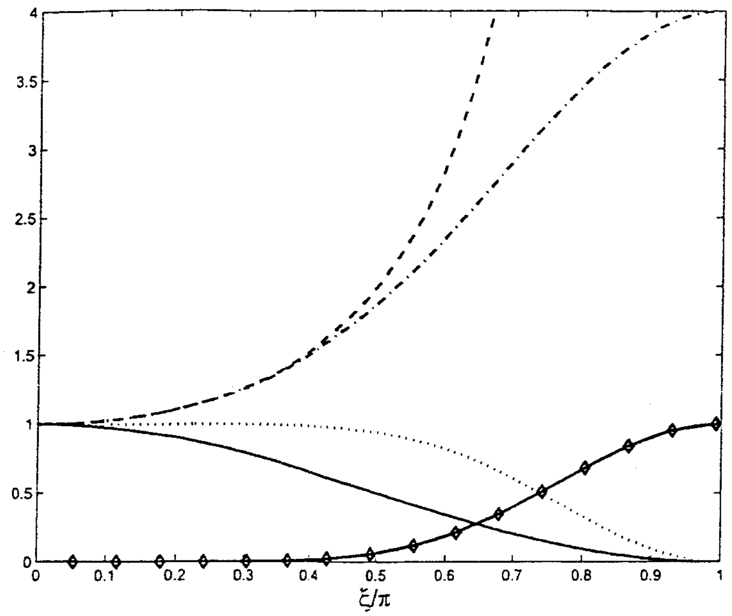

Figure 1: Transfer function of second-order Padé filter, its exact inverse, its approximate inverse, and related operators. LEGEND: $H$ (solid), $H^{-1}$ (dashed), $H_3^{-1}$ (dashed and dotted), $H * H_3^{-1}$ (dotted), and $1 - H * H_3^{-1}$ (solid with symbols).

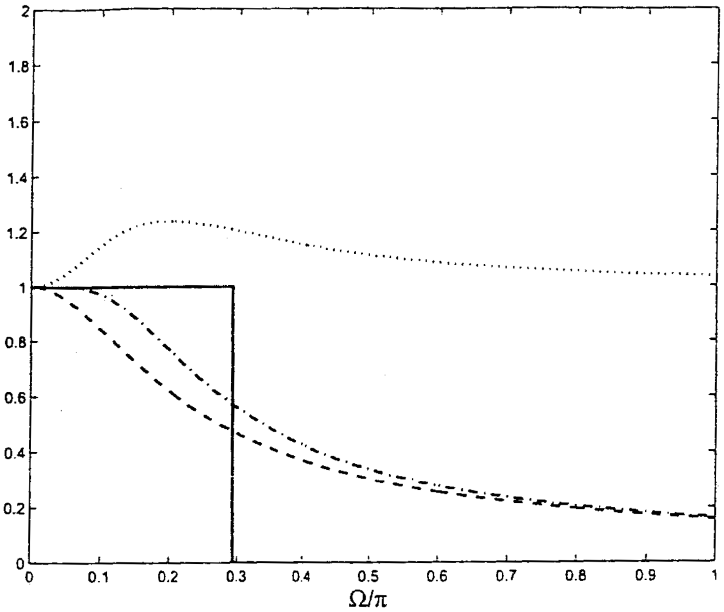

Figure 2: Transfer functions for $H$ (dashed), $\tilde{H}^{-1}$ (dotted), $H * \tilde{H}^{-1}$ (dashed and dotted), and spectral function (solid) for a third-order deconvolution with coefficients $[1.0, 0.559, -0.784, 0.225]$ and $r = 2$.

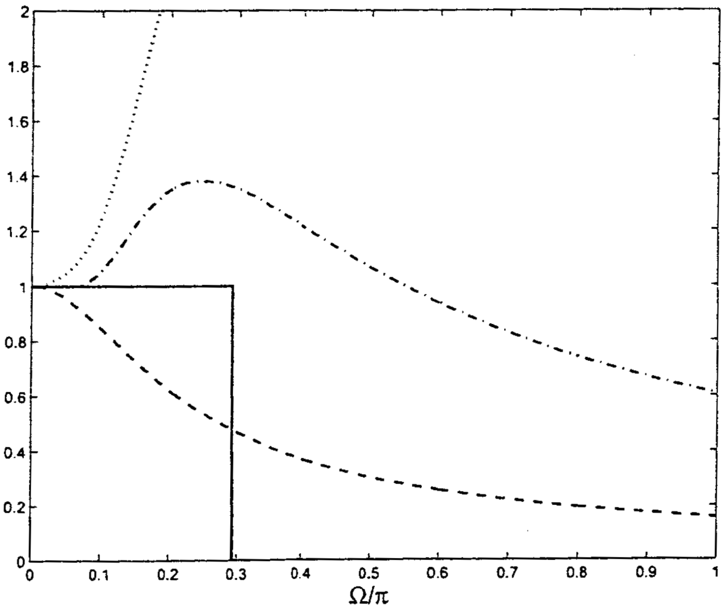

Figure 3: Transfer functions for $H$ (dashed), $\tilde{H}^{-1}$ (dotted), $H * \tilde{H}^{-1}$ (dashed and dotted), and spectral function (solid) for a third-order deconvolution with Pascal coefficients $[4, -6, 4, -1]$ and $r = 2$.

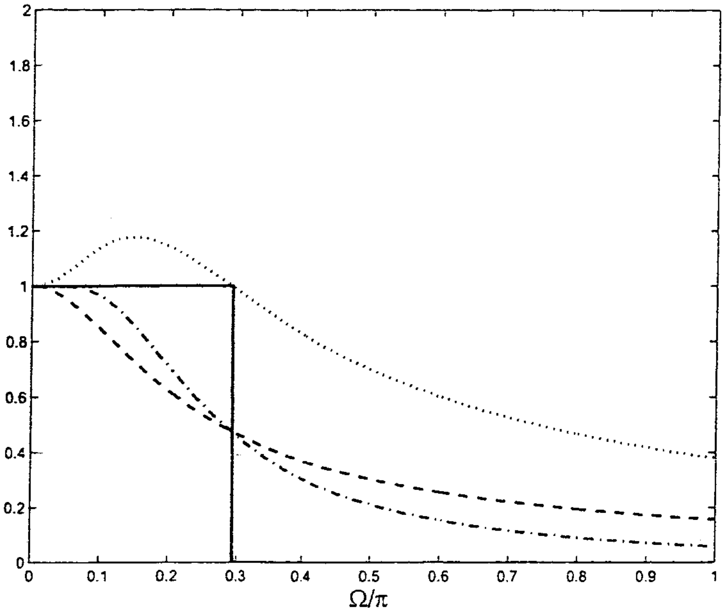

Figure 4: Transfer functions for $H$ (dashed), $\tilde{H}^{-1}$ (dotted), $H * \tilde{H}^{-1}$ (dashed and dotted), and a spectral function (solid) for third-order deconvolution with optimized coefficients $[0.0, 2.4495, -1.9159, 0.4664]$ and $r = 2$.

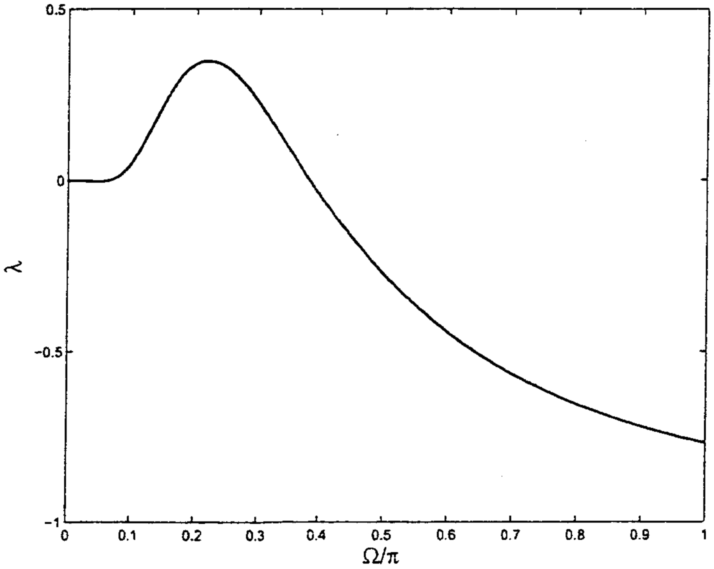

Figure 5: Decay rate ($\lambda$) for third-order deconvolution with Pascal coefficients $[4, -6, 4, -1]$, $r = 2$, and $\chi = 1.0$.

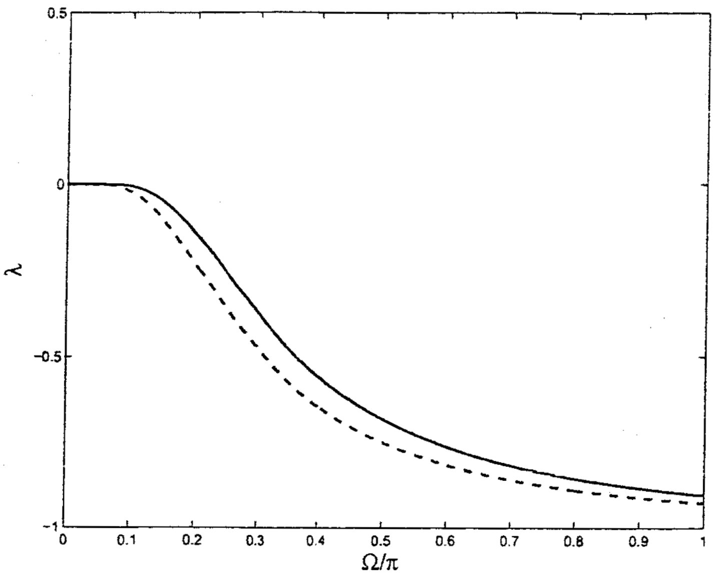

Figure 6: Decay rates ($\lambda$) for third-order and second-order deconvolutions with optimized coefficients $[2.1875, -1.8125, 0.75, -0.125]$ and $[1.875, -1.125, 0.750]$, respectively, $r = 2$, and $\chi = 1.0$. LEGEND: $p = 3$ (solid); $p = 2$ (dashed).

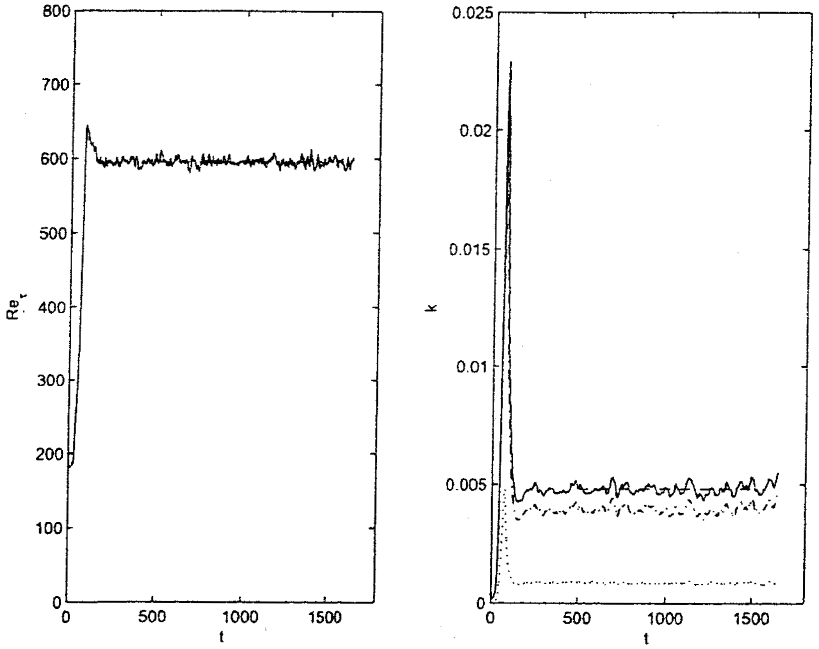

Figure 7: Evolution of $Re_\tau$ and $k$ for Case TLES590. LEGEND: solid line (instantaneous); dashed line (mean); dashed-dotted line ($\bar{k}$); dotted line ($k_R$).

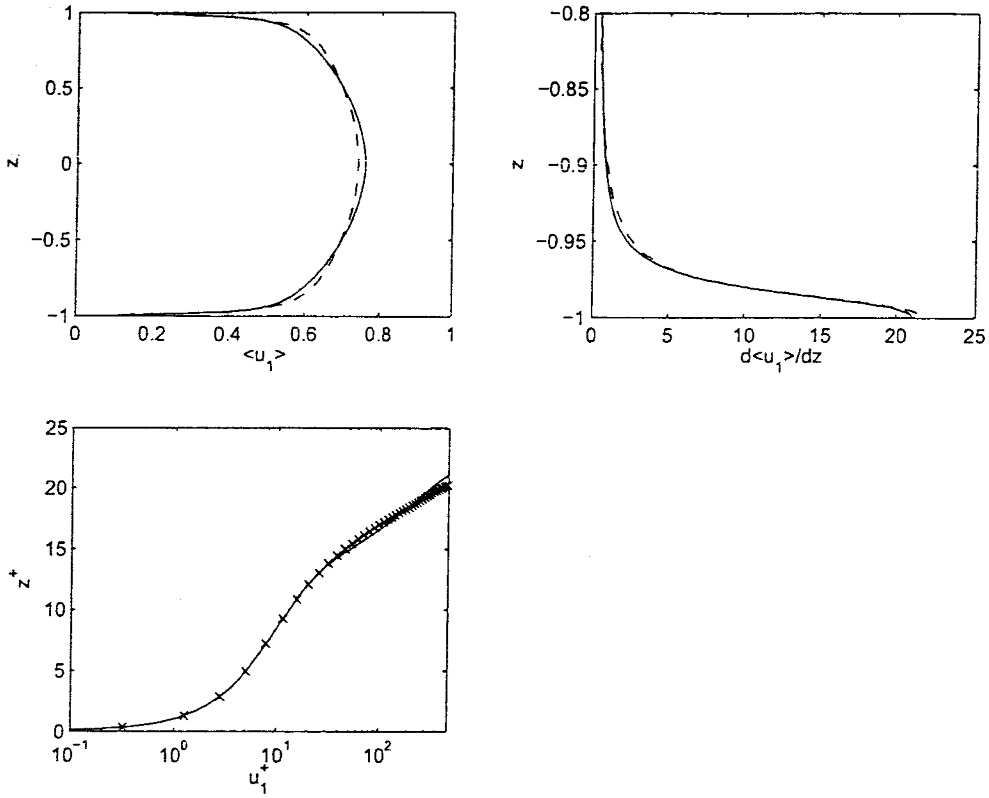

Figure 8: Mean streamwise velocity profile $< u_1 >$ vs. $z$ and its wall-normal derivative for Case TLES590 relative to reference DNS data of Moser et al. LEGEND: solid line (KMM); dashed line (TLES590); symbols (TLES590, wall units).

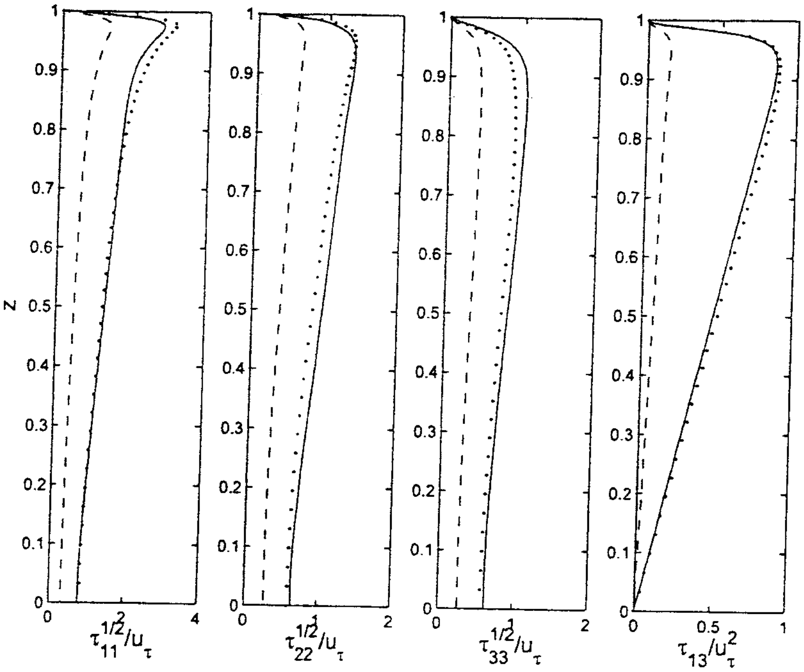

Figure 9: Fluctuation velocities and Reynolds stresses vs. $z$ for Case TLES590 relative to reference DNS data of Moser et al. LEGEND: solid line (reference DNS); dotted line ($< M_{ij} > + \bar{\tau}_{ij}$, TLES); dashed line (contribution of $< M_{ij} >$, TLES).